T2380

EFFECTS OF LIQUID LITHIUM ON FATIGUE CRACK PROPAGATION IN 304L STAINLESS STEEL

by

DUNCAN LYLE HAMMON

CLOSED RESERVE

COLORADO SCHOOL OF MINES
GOLDEN, COLORADO

ProQuest Number: 10782201

All rights reserved

INFORMATION TO ALL USERS
The quality of this reproduction is dependent upon the quality of the copy submitted.

In the unlikely event that the author did not send a complete manuscript
and there are missing pages, these will be noted. Also, if material had to be removed,
a note will indicate the deletion.

ProQuest 10782201

Published by ProQuest LLC (2018). Copyright of the Dissertation is held by the Author.

All rights reserved.
This work is protected against unauthorized copying under Title 17, United States Code
Microform Edition © ProQuest LLC.

ProQuest LLC.
789 East Eisenhower Parkway
P.O. Box 1346
Ann Arbor, MI 48106 – 1346

T2380

A thesis submitted to the Faculty and the Board of Trustees of the Colorado School of Mines in partial fulfillment of the requirements for the degree of Master of Science-Metallurgical Engineering.

Golden, Colorado

Date: August 14, 1980

Signed: Duncan L. Hammon

Duncan L. Hammon,
Student

Approved: David K. Matlock

David K. Matlock,
Thesis Advisor

Golden, Colorado

Date: August 14, 1980

William D. Copeland,
Head of Department

ABSTRACT

The effects of a liquid-lithium environment and frequency on the fatigue-crack-propagation characteristics of 304L stainless steel were investigated. At 973K, the crack-propagation rate was higher in lithium containing 2000 ppm nitrogen than in argon containing 200-300 ppm oxygen and 1400-2000 ppm nitrogen. The increased propagation rate in lithium was accompanied by a change in propagation mode from transgranular in argon at 20 and 1.7 Hz to intergranular in lithium. Intergranular propagation was observed in all specimens tested at 0.067 Hz. The increase in propagation rate and the transition to intergranular propagation in lithium was attributed to strain-enhanced, grain boundary penetration at the crack tip.

TABLE OF CONTENTS

LIST OF FIGURES

ACKNOWLEDGEMENTS

The author acknowledges the United States Department of Energy for financial support of this research program. The education and guidance of the faculty, especially Dr. D. K. Matlock and Drs. D. L. Olson and G. R. Edwards, is greatly appreciated.

I would also like to express my appreciation to my family; especially my wife, Diane; for their support throughout my education.

INTRODUCTION

The purpose of this investigation is to determine the effect of a liquid lithium environment on the fatigue crack propagation characteristics of 304L stainless steel at elevated temperatures. An understanding of the nature of stress/environment interactions is essential because lithium is known to be corrosive and because stress and corrosion processes have been shown to interact under many circumstances. The main impetus behind this investigation, as well as other lithium corrosion research, is the potential use of liquid lithium as a heat transfer medium in advanced energy production systems. Like sodium, the physical properties of lithium make it particularly attractive for such applications.

To better understand the results of this investigation, it is important to understand the results of

previous studies of the corrosion of materials in liquid lithium as well as the several types of stress/environment interactions observed in other well documented systems. The most common low temperature interactions are stress-corrosion cracking, corrosion fatigue, liquid-metal embrittlement and several forms of hydrogen damage. High temperature creep and fatigue interactions are of particular interest. An understanding of the mechanical nature of fatigue crack propagation in the absence of environmental effects is also very important if the effects of lithium are to be isolated.

BEHAVIOR OF MATERIALS IN LIQUID LITHIUM

The behavior of materials in molten lithium has been investigated extensively and the results have been reviewed in several publications (1,2,3). Most of these investigations involved the corrosion of unstressed specimens submerged in lithium under static, isothermal conditions (4,5,6,7). Other studies involved lithium flowing through forced (pumped) or convection loops (8). In addition to these investigations, lithium attack on specimens subjected to stress has been reported by a few workers (9,10,11).

A review of the stress/corrosion interactions reported for liquid sodium systems is included at the end of this section. Because of the chemical and physical similarities of lithium and sodium, knowledge of the effects of sodium on engineering materials under stress will be useful in the interpretation of the behavior of materials in liquid lithium.

Behavior of Unstressed Materials

The two most common forms of attack observed in unstressed coupons in static lithium systems are 1) general surface attack in which the material is removed uniformly

from the surface either by a selective dissolution or a general dissolution process; and 2) grain boundary penetration, a highly localized attack in which the lithium penetrates along grain boundaries with or without general surface attack. These two forms of corrosion are illustrated schematically in Figure 1. Experimentally, general surface attack is measured as weight loss per unit surface area and the depth of grain boundary penetration is determined by examining cross sections of corroded specimens by optical metallography.

Selective dissolution of nickel in lithium has been shown to lead to the formation of a porous surface layer in the high nickel alloy RA 333 (12) and to cause the surface of 304L stainless steel to transform to ferrite (13). General surface attack of 304L stainless steel has been shown to follow a parabolic time dependence as described by the following equation (4):

$$W=(k_W t)^{1/2} \qquad [1]$$

where W is weight loss/area, t is time, and k_W is the weight loss rate coefficient. Reser (4) developed the following empirical relation for k_W in terms of nitrogen concentration in the lithium and temperature:

$$\text{above 727C: } k_W=22.3\times10^{-8}[N]^{2.5}\exp\{-17000/RT\} \qquad [2a]$$

$$\text{below 727C: } k_W=24.2\times10^{-8}[N]^{2}\exp\{-17000/RT\} \qquad [2b]$$

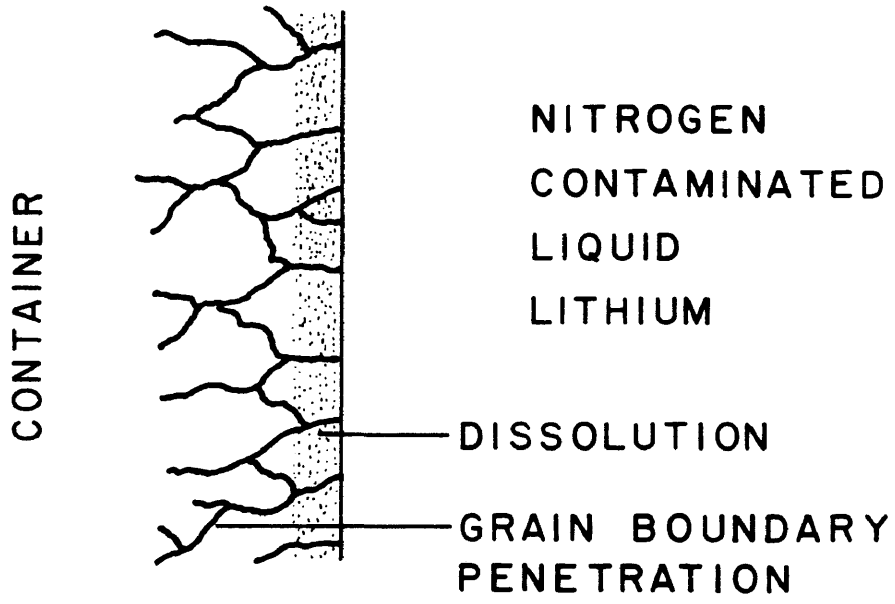

Figure 1. A schematic illustration of the general dissolution and grain boundary penetration commonly observed in materials exposed to nitrogen contaminated lithium (from Olson and Matlock, ref.1).

where N is the nitrogen concentration in weight percent, T is the absolute temperature, and R is the gas constant in calories. Time, t, in hours gives the weight loss in grams per square millimeter. The importance of dissolved nitrogen in the lithium is apparent. These equations show that the corrosion kinetics can be greatly reduced by maintaining low nitrogen levels.

Reser (4) also developed the following expressions to describe the grain boundary penetration of 304L stainless steel submerged in liquid lithium:

$$P=(k_p t)^{1/2}, \quad [3]$$

above 727C: $k_p = 2.8[N] \exp\{-17000/RT\}$ [4a]

below 727C: $k_p = 4000[N]\exp\{-31000/RT\}$ [4b]

where P is the depth of penetration in millimeters and the other terms are defined as before. Once again, the importance of nitrogen is apparent.

Reeves (14) demonstrated the lack of mechanical integrity associated with penetrated grain boundaries by bending a specimen which had been previously exposed to lithium attack. The result of this bend test, shown in Fig. 2, suggested that a relationship between stress and lithium corrosion might exist.

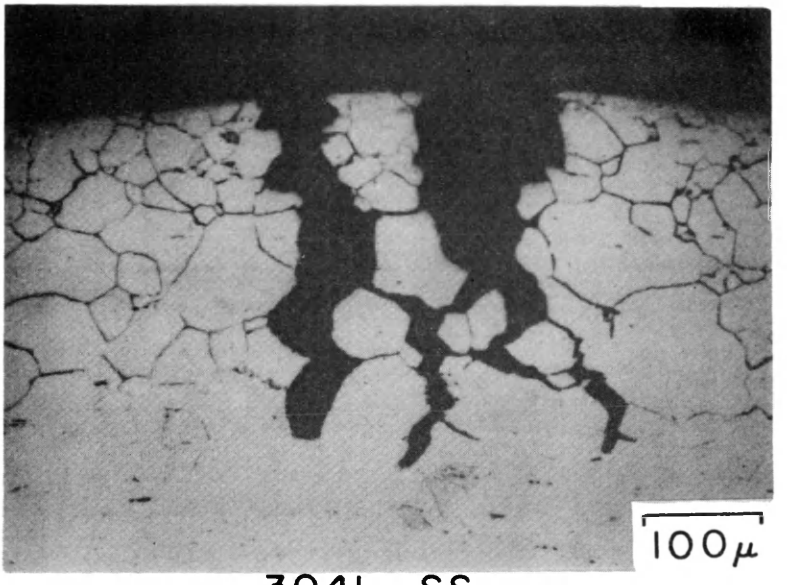

Figure 2. Optical micrograph illustrating the lack of mechanical integrity associated with penetrated grain boundaries in a 304L stainless steel specimen which was bent after exposure to lithium (from Reeves et al, ref.7).

Behavior of Stressed Materials

Jordan et al (9) performed constant load creep tests on Armco iron submerged in molten lithium to determine the effect of an applied stress on lithium attack. Isochronal plots of penetration as a function of stress, reproduced in Fig. 3, illustrate the stress enhancement of grain boundary penetration in a material which experiences very little attack when exposed to lithium in the absence of a stress. Whipple (10) extended this study by comparing the effect of compressive and tensile stresses on grain boundary penetration during steady state creep of Armco iron submerged in lithium. Plotting penetration as a function of time, as in Fig. 4, shows that either a tensile or a compressive stress greatly increases the penetration which again is a parabolic function of time. Furthermore, Whipple showed the penetration rate coefficient to be proportional to the creep rate. In steady state creep the strain rate is constant so penetration is proportional to the total strain to the one-half power.

On the basis of these results, a strain-enhanced corrosion model was proposed. It was suggested that slip along planes intersecting grain boundaries fractured a corrosion product layer exposing new material which corrodes very rapidly.

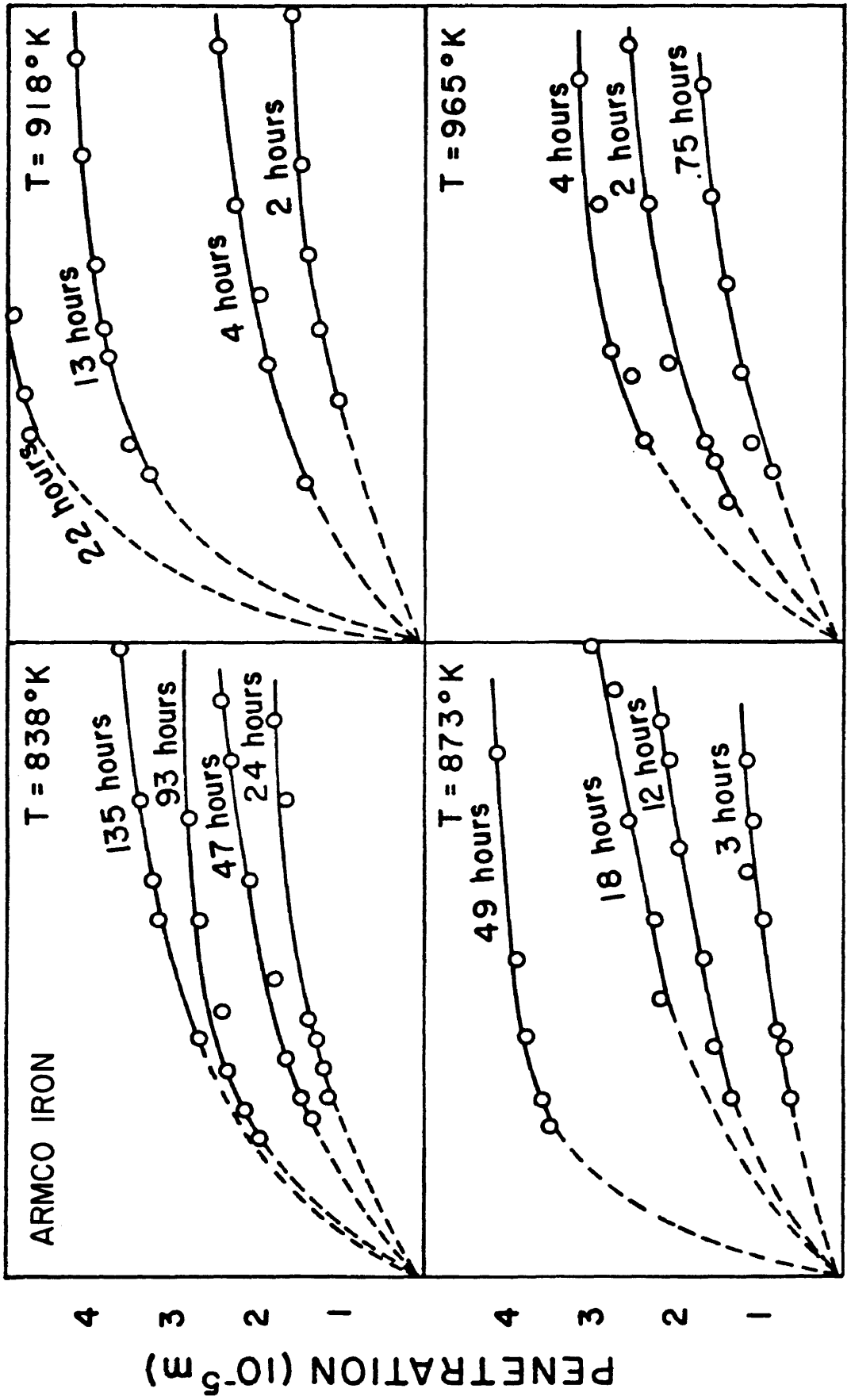

Figure 3. Isochronal plots of penetration as a function of stress for Armco iron subjected to creep in liquid lithium (from Jordan et al, ref.9).

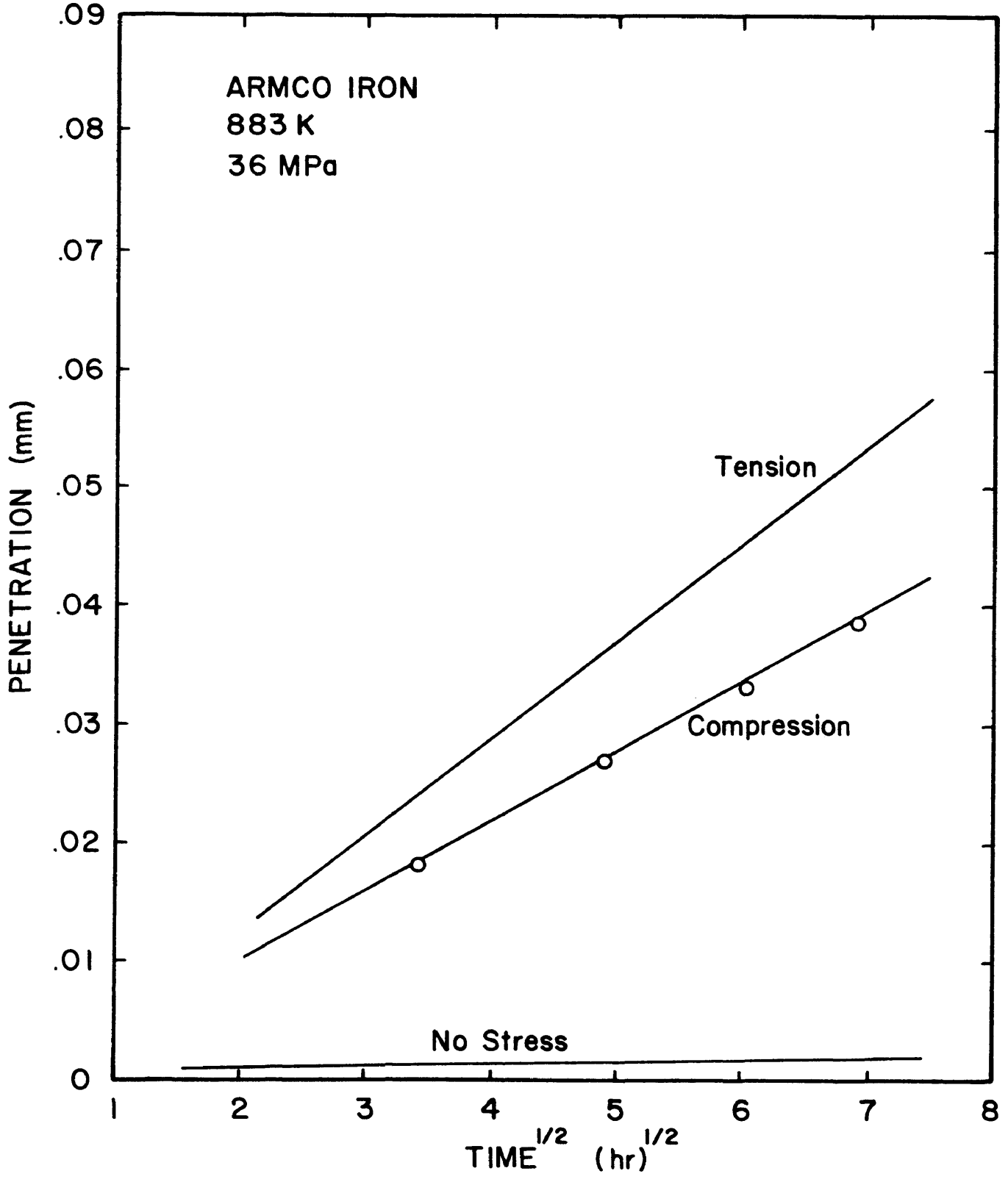

Figure 4. Penetration as a function of the square root of time for Armco iron subjected to creep in tension and compression in liquid lithium (from Whipple et al, ref.10).

In a separate investigation, Kustas (11) measured grain boundary penetration during torsional fatigue of Armco iron in liquid lithium. It was thought that if penetration depended on plastic deformation, then the extremely large strains accumulated during the torsion testing would greatly enhance penetration. Enhanced penetration was observed but it was found to be a linear function of time and to be proportional to the total strain accumulated during the test. It was proposed that the controlling step for penetration was not deformation as in the case of steady state creep. Instead, the transport of liquid lithium along grain boundaries and other deformation zones was proposed as the rate controlling step.

The effect of nitrogen on the stress/corrosion behavior observed in the aforementioned studies has not been investigated. Kustas (11) reported a nitrogen level of approximately 600 ppm for each of the tests during his investigation. Equations [1] to [4] show the nitrogen level to be very important in the static corrosion of 304L stainless steel, but this may not be the case for the corrosion of material subject to an applied stress.

Popovich et al (15) and Chaevski et al (16) have reported decreases in the ultimate tensile strength of hollow Armco iron tensile specimens when filled with

lithium in the 300 to 1000C temperature range. The effect was most pronounced near 300C but the ductility was reduced by 40 percent even at 800C. In a study of the effects of lithium on the tensile properties of an austenitic stainless steel, Popovich et al (17) reported that the ultimate tensile strength was not affected at a deformation rate of 8mm/min but the elongation was greatly reduced when tested at 0.13mm/min at 900C. An important result of this investigation was that an addition of 1 percent nitrogen to the lithium had no effect on the mechanical properties although grain boundary penetration increased. These results demonstrate the complexity of lithium attack.

Stressed Materials in Liquid Sodium

The behavior of materials in liquid sodium has been investigated extensively, primarily due to the use of sodium as a nuclear reactor coolant. Results of liquid sodium corrosion research, particularly under stressed conditions, might be useful in the understanding of lithium stress/corrosion interactions because of the similarities in physical properties and in potential applications.

Several investigators have examined the effect of sodium on the creep behavior of engineering materials (18,19,20). Samples were exposed to sodium prior to or

during testing. Exposure of austenitic stainless steels to sodium prior to testing can increase the creep rupture life if carbon diffuses from the sodium into the steel (20). If, on the other hand, the carbon potential in the sodium is low, decarburization will occur with a corresponding decrease in creep rupture life.

The presence of sodium during creep had little effect on the steady state creep of stabilized (with respect to carbon) austenitic stainless steels (18). Sodium did lower the total elongation to fracture but without significantly changing the rupture life. Rapid corrosion along slip bands was observed and the liquid sodium promoted intergranular fracture.

Flagella and Kahrs (21) found the fatigue life of type 316 stainless steel in sodium to be the same as in air during high stress, low-cycle fatigue. Fatigue life in sodium was greater than in air for low stress, high-cycle fatigue. This was attributed to oxidation during fatigue in air. Smith et al (22) also found the fatigue life of 316 stainless steel in sodium higher than in air at 600C. The fatigue life of 304 stainless steel was unaffected by the sodium when compared to air.

In addition to the fatigue life studies mentioned previously, James and Knecht (23) measured crack growth

rates as a function of effective stress intensity for 304 stainless steel in liquid sodium and compared these to growth rates in air and in vacuum. At 427C and 538C the growth rates in sodium and in vacuum were very similar and both were considerably lower than those in air. Once again this behavior was attributed to oxidation in air and demonstrated the relatively inert behavior of low oxygen sodium.

These observations show that the oxygen and carbon levels in liquid sodium are very important parameters which influence the effect of sodium on the behavior of metals. This is analogous to nitrogen in liquid lithium as mentioned previously: The degradation of material properties in sodium can be eliminated if the oxygen content is very low (and decarburization does not occur) as may be the case for nitrogen in liquid lithium.

REVIEW OF STRESS/ENVIRONMENT INTERACTIONS

As alluded to earlier, an understanding of stress/environment interactions in other systems may be helpful in understanding the results of this investigation. For the purpose of this thesis, these interactions have been divided into low and high temperature phenomena and will be reviewed below. Included under low temperatures are stress-corrosion cracking, corrosion fatigue, liquid-metal embrittlement, and hydrogen damage. Creep and high temperature fatigue are included in the high temperature phenomena.

Low Temperature Interactions

Stress Corrosion Cracking. Stress-corrosion cracking (SCC) is environment-assisted crack growth under static loading. It occurs in particular metal/environment systems when the local tensile stress (characterized by the stress intensity factor, K) exceeds a critical value (24). This critical stress intensity, K_{SCC}, is a function of alloy, heat treatment, temperature, and the concentration of critical species in the environment. Stress-corrosion cracking occurs in aqueous and gaseous environments.

Cracks propagate at loads significantly less than those which would be required in inert environments. Both intergranular and transgranular SCC are observed with crack branching frequently occurring (25). Stress-corrosion cracking is differentiated from other types of environment-assisted cracking in that an electrochemical corrosion process must be occurring , hence, SCC can be prevented by cathodic protection (25).

Bursle and Pugh (26) have evaluated current SCC models on the basis of fractographic evidence. They conclude that transgranular SCC is best described by a bulk-embrittlement model although selective dissolution is a possible alternative. Intergranular SCC, however, is attributed to a mechanism described as film-rupture. The film-rupture mechanism is shown schematically in Fig. 5. Slip during stress relaxation at the tip of the crack ruptures the protective film, allowing rapid dissolution to occur.

Aside from the fact that SCC is generally limited to low temperatures, SCC can not explain the effect of stress on lithium atack mainly because it requires a local tensile stress whereas compressive stresses also enhance grain boundary penetration in liquid lithium. However, the similarity between the mechanism proposed by Whipple et al (10) and the film-rupture mechanism is very apparent.

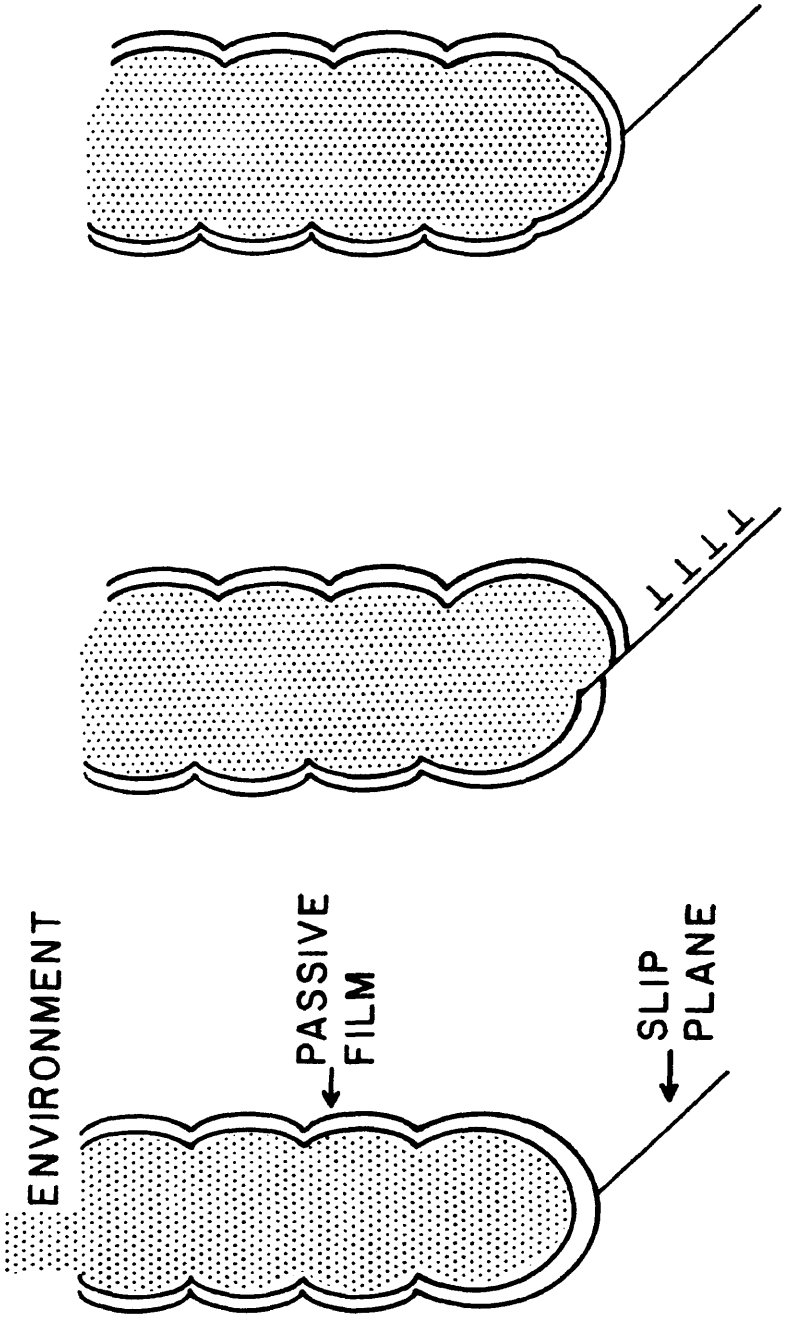

Figure 5. A schematic representation of the film-rupture model for stress-corrosion cracking. Slip at the crack tip ruptures the passive film allowing rapid dissolutioin until repassivation occurs (after Bursle and Pugh, ref.26).

Corrosion Fatigue. Corrosion fatigue may be defined as the reduction in fatigue resistance due to the presence of a corrosive medium (25). Environments which influence fatigue properties are not limited to those which are aggressive under static conditions, however. For example, water vapor and air have been shown to adversely affect the room temperature fatigue properties of many metals while not significantly altering static properties.

Duquette (27), in a review of the mechanisms of corrosion fatigue, considers fatigue in gaseous environments separate from aqueous environments. Oxygen is the primary species of concern in gaseous environments although it certainly is not the only gas which can affect fatigue properties (for example see reference 28). Duquette concludes that increased crack growth rates can be attributed to interference with slip reversibility which occurs above a critical adsorbed concentration of gas at the crack tip. In aqueous environments rapid corrosion occurs along slip bands aiding crack initiation and propagation. Also, alloys which are susceptable to hydrogen embrittlement may be adversely affected by hydrogen evolved during corrosion in the crack. Pao et al (29) attribute the acceleration of crack growth rates in

4340 steel in water vapor to hydrogen embrittlement. The growth rate was found to be inversely proportional to the frequency which was explained in terms of the time necessary to produce a critical hydrogen concentration.

Lynch (30) proposes a model for environmentally enhanced fatigue crack propagation in which certain species adsorb at the crack tip. This adsorption reduces the lattice distortion in the metal surface making the generation and egress of dislocations easier. This would promote slip on a few planes at the crack tip compared to general slip in a large plastic zone. Concentrated slip would in turn promote crack propagation by concentrating damage acumulation at the crack tip. Lynch suggests that liquid metals should be very effective in increasing crack growth rates due to the electronic similarity between the solid and liquid metal atoms.

Liquid-Metal Embrittlement. Of particular interest in this thesis are stress/liquid-metal environment interactions. Liquid-metal embrittlement (LME) refers to a phenomena in which severe degradation of the mechanical properties (ductility and fracture strength) of a metal occurs in the presence of a liquid metal. Embrittlement by solid metals has also been observed; apparently by the same

mechanism (31). LME occurs in specific systems and combinations of temperature and strain rate. It is apparent that LME is different from many environmental effects in that normal corrosion or dissolution processes need not occur although intimate contact between the propagating crack tip and the embrittling species is necessary.

Many empirical observations concerning the effects of LME as well as the physical and chemical characteristics of embrittling couples have been made (32). These observations can be used to evaluate models both in terms of predicting and explaining the observed behavior.

1) The effects of LME are observed over a narrow temperature range near the melting point of the embrittling species for both LME and solid-metal embrittlement;

2) The deformation characteristics of the solid metal (ie. strain-hardening rate and yield strength) are unaffected up to the fracture point;

3) The fracture may be intergranular or transgranular;

4) Analysis of the specific couples in which LME has been observed suggests the following criteria

which, if met, increase the likelihood of LME being observed;

a) the metals exhibit little mutual solubility,

b) the metals do not form stable intermediate compounds.

The observation that embrittlement is favored when the electronegativities of the couple are nearly the same may be regarded as a more quantitative statement of b) above.

Currently, the most widely accepted model for LME involves the reduction in bond strength resulting from the adsorption of embrittling atoms at a crack tip. The reduction in surface energy as a result of liquid-metal wetting cannot account for the magnitude of LME although the surface energy and bond strength are closely related as shown in the equation from Kelly (33):

$$\sigma_{max} = E\gamma^{1/2}/a_o \qquad [5]$$

where a_o is the interatomic spacing, E is the elastic modulus, γ is the surface energy, and σ_{max} is the bond strength.

Kamdar (32) has applied a model presented by Kelly (33) for the conditions necessary for completely brittle behavior, to the adsorption induced lowering of bond strength model for LME. Kelly proposes that totally

brittle fracture can occur if the maximum tensile stress (σ_a) reaches the fracture stress (σ_{max}) before the maximum shear stress (τ_a) reaches the theoretical shear strength of the material (τ_{max}). More concisely, brittle fracture can occur if

$$\frac{\sigma_a}{\tau_a} > \frac{\sigma_{max}}{\tau_{max}} \quad . \qquad [6]$$

This inequality was initially applied to an isotropic continuum assuming that no thermally activated slip occurs. However, the basic idea of the maximum tensile stress exceeding a critical value before slip occurs is very useful in interpreting and predicting brittle fracture in engineering materials.

The ratio σ_a / τ_a is primarily a function of the stress state and also the crystal system which determines the relationship between the slip direction and the cleavage plane (or the grain boundary if intergranular fracture occurs). For a plane strain condition, where the tensile stress perpendicular to the crack plane is equal to the tensile stress in the direction of crack propagation, σ_a/τ_a varies from 2.86 (for Poisson's ratio equal to 0.15) to 12.50 (for $\nu = 0.42$) (33). For brittle fracture to occur according to Equation [6] then, $\sigma_{max} / \tau_{max}$ must be less than about 10.

The environmentally sensitive parameter is σ_{max} with τ_{max} being a function of the particular material. The shear strength is considered a bulk property and is not affected by surface reactions. The fracture strength, σ_{max}, however, is a property of the bonds at the crack tip where the fracture process is occurring and is, therefore, environmentally sensitive. Theoretical calculations of σ_{max}/τ_{max} in an inert environment range from 33.8 for FCC gold to 5.04 and 6.75 for BCC tungsten and iron, respectively(33). Comparing these values to those for σ_a/τ_a suggests that FCC materials should not cleave whereas BCC materials may fail by cleavage in the absence of any dislocation motion.

Kamdar (32) proposes that the embrittling species reduces the bond strength, and therfore σ_{max}, at the crack tip without altering τ_{max}. For a given applied σ_a/τ_a, the liquid metal promotes brittle behavior by reducing σ_{max}/τ_{max} to a value below σ_a/τ_a. This model predicts that the severity of LME should be accentuated by factors which promote brittle behavior. These factors include planar slip, low temperatures, high strain rate, high hydrostatic tensile stresses at a crack tip, and high strength.

Hydrogen Damage. Aside from being another form of

stress/environment interaction, hydrogen damage is included here because the characterics of, and proposed mechanisms for, one form of hydrogen damage are similar to those of liquid-metal embrittlement and may, therefore, be pertinent to this investigation. The first two forms, namely high pressure bubble formation and hydride formation, are included primarily for completeness although all forms of hydrogen damage can affect mechanical properties.

One form of hydrogen damage results from the formation of high pressure (up to 10^5 atm) hydrogen bubbles near external surfaces (34). These "flakes" or "blisters" can only form when the activity of hydrogen in the environment is very high; it must be higher than in the flake. A similar phenomena is observed in many alloys containing carbon or oxygen. In such alloys, hydrogen diffuses into the material and reacts to form high pressure gas bubbles. The formation of methane at cementite particles is one example of such a reaction (35).

Hydride formation is one of two forms of hydrogen damage which are solid state phenomena (no gases are produced) and are more accurately described as hydrogen embrittlement. It occurs when dissolved hydrogen reacts to form a brittle hydride which in turn fractures in a brittle manner under an applied tensile stress (34). The hydride

formed may be thermodynamically stable at the pressure and temperature of the system or it may be strain-induced in systems where localized strains at a crack tip promote hydride formation.

The second form of hydrogen embrittlement reduces the ductility of the material and occurs without the formation of a second phase. It occurs when low levels of hydrogen are dissolved in a susceptable material. The mechanism of this form of embrittlement is not well understood but two closely related explanations for the observed behavior suggest a close relationship to liquid-metal embrittlement. These are: 1) reduction of surface energy due to the adsorption of hydrogen on the fracture surface, and 2) decohesion or the reduction in bond strength at the tip of the crack due to dissolved or adsorbed hydrogen. These models were discussed in greater detail with respect to LME. In either case, hydrogen diffusion to --or generation at-- a crack tip appears to be the controlling process as embrittlement can be avoided by high strain rates and low temperatures.

High Temperatures Interactions

High temperature deformation is characterized by time dependent processes including dislocation climb and grain

boundary sliding. These processes, along with high reaction rates (ie.oxidation), separate the effects of environment at high temperature from the low temperature effects.

Creep/Environment. Possible environmental effects during high temperature creep are reviewed by Cook and Skelton (36). These effects extend beyond crack propagation as the steady state creep rate is also influenced. Increasing the partial pressure of oxygen has been shown to increase or decrease the creep rate depending on the alloy, temperature, and oxygen pressure. Grain boundary oxidation may inhibit grain boundary sliding or an adherent oxide may bridge existing surface cracks, either of which could decrease the creep rate. The formation of sub-surface second phase particles by internal oxidation, nitriding, or carburizing generally reduces the creep rate. Extensive uniform oxidation in cases where the oxide is not adherent decreases the cross sectional area and subsequent deformation may enhance oxidation. Loss of alloying elements to the environment (ie. decarburization) generally increases the creep rate by decreasing the strength of the material.

High Temperature Fatigue. Environmental effects during high temperature fatigue are obviously important to this investigation. High temperatures rule out aqueous environments usually making gaseous environments of primary concern although molten salts and liquid-metal environments are more important to this investigation.

Before the effects of environment can be understood, the mechanisms of both low temperature and high temperature fatigue crack propagation must be understood. At low temperatures, crack propagation occurs by a plastic blunting process (37). This process is illustrated in Fig. 6 which is a schematic drawing of a crack tip at several stages of a loading cycle. As the load is applied, the crack extends by plastic shearing and becomes more blunt (Fig. 6 (a) to (c)). When the load decreases, the crack tip goes into compression and the crack is resharpened (Fig. 6 (d) and (e)). The process is repeated as the load again increases as in (f).

At elevated temperatures, time dependent creep processes can interact with the cycle dependent processes observed at low temperatures. Grain boundary sliding and grain boundary void growth are time-dependent, intergranular fracture processes which occur throughout the plastic zone ahead of the crack tip and which contribute to

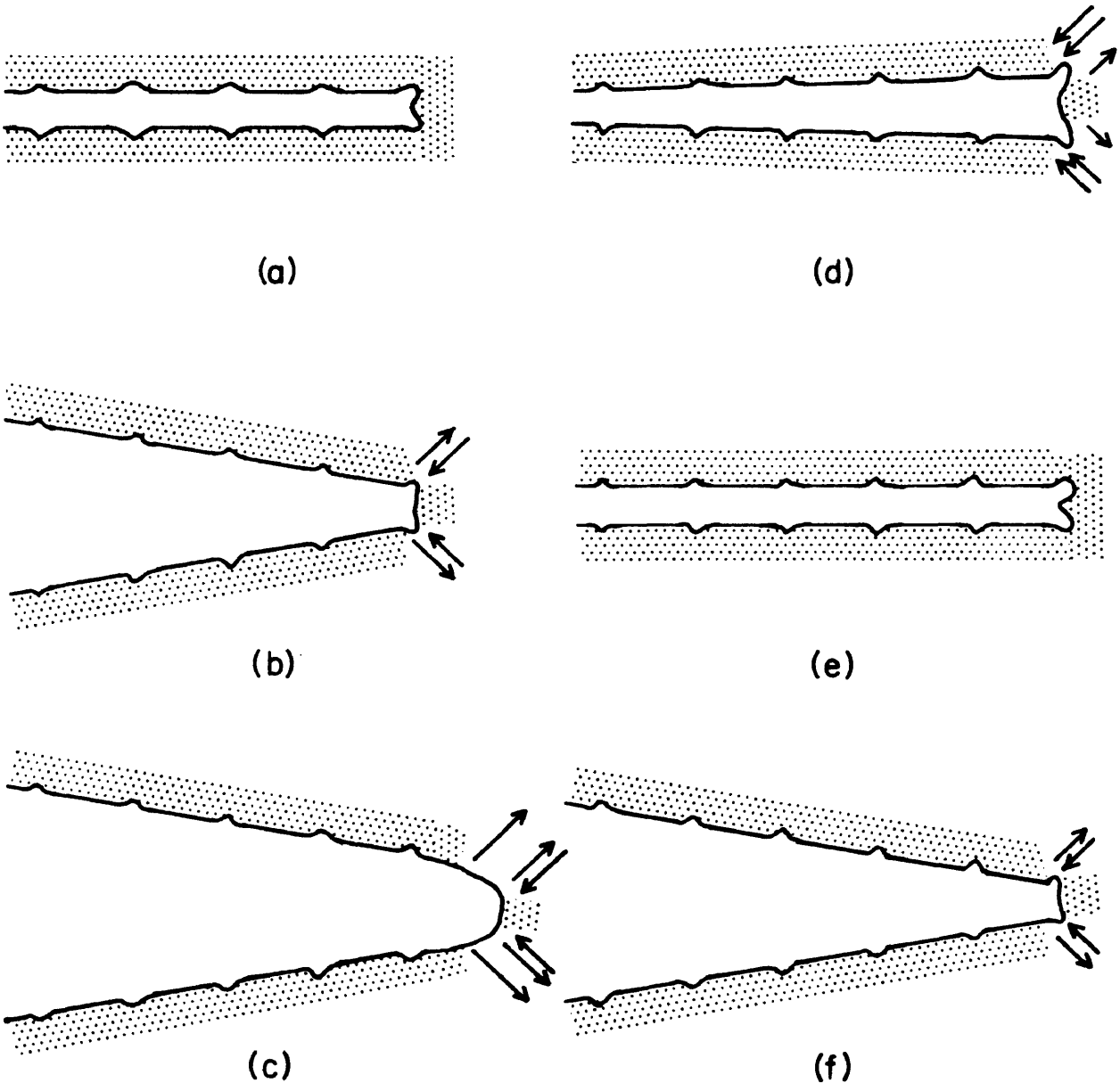

Figure 6. A schematic illustrating fatigue crack propagation by local plasticity at a crack tip. The fatigue crack (a) opens as the applied load is increased (b) and extends by plastic blunting of the crack (c). The crack is resharpened on unloading (d) with the crack length having increased at the minimum load (e). The process is then repeated (f) (after Laird, ref.37).

crack propagation by grain boundary separation. Because these processes are time dependent, they contribute more to the total deformation as the frequency decreases (time at load per cycle increases) causing intergranular crack propagation at low frequencies and high temperatures.

Environmental interactions during high temperature fatigue are generally more severe than those during creep, primarily due to the large cyclic strains imposed at the crack tip. Also, incidences of increased fatigue life attributable to oxidation have not been reported. The degree of fatigue/environment interaction should also depend on frequency as corrosion processes are certainly time dependent.

Figure 7, which is a plot of crack growth rate vs. frequency, illustrates the effect of frequency and environment on the fatigue crack propagation characteristics of A286 steel at 1100 F (38). As the frequency decreases, the creep component contributes more to the deformation and crack propagation changes from transgranular to intergranular in both vacuum and in air. The effect of the air environment is to promote intergranular propagation at higher frequencies and to increase the growth rate.

Figure 7 emphasizes that when considering high

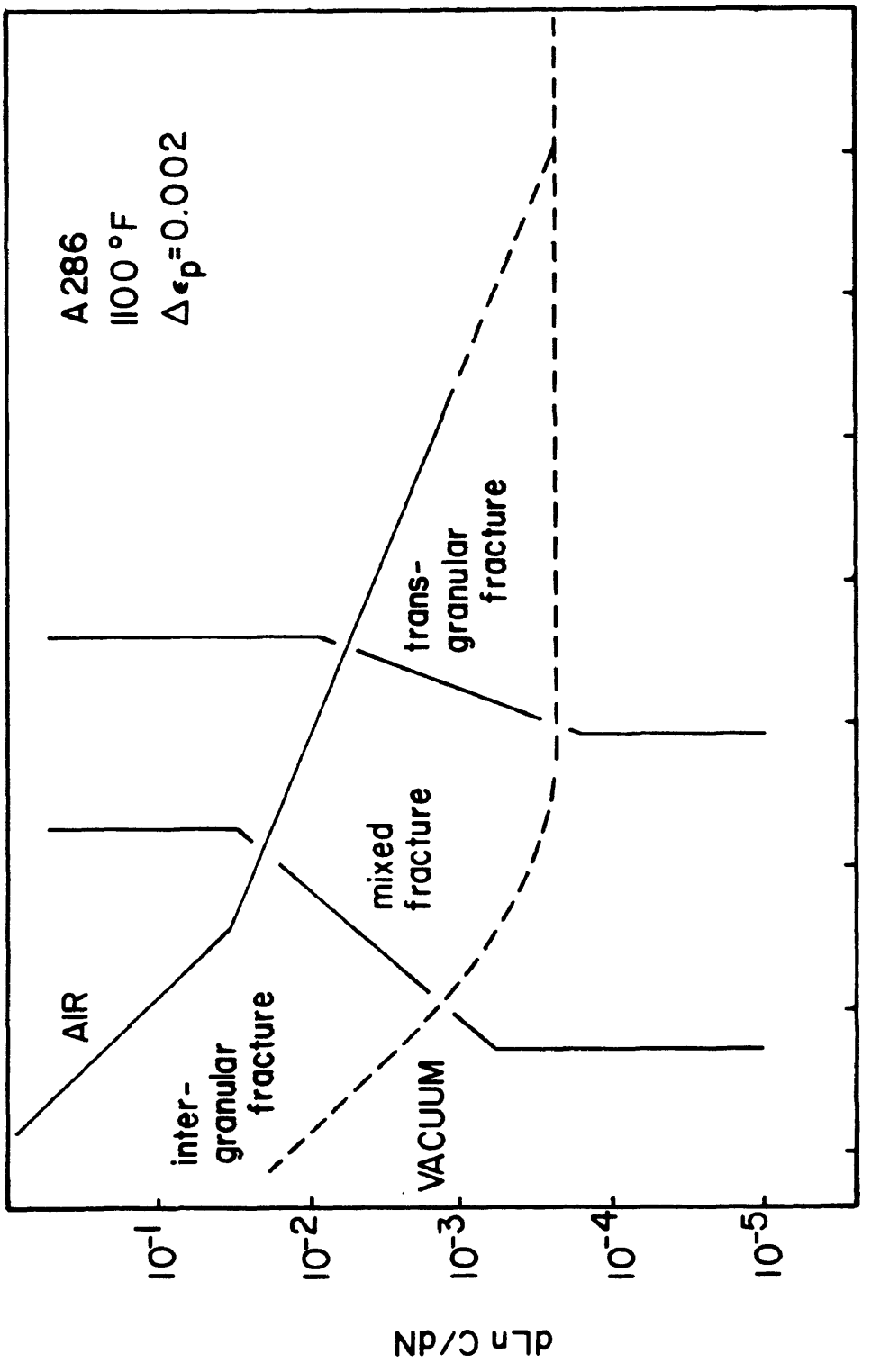

Figure 7. The effects of frequency and environment on the rate and mode of fatigue crack propagation in A286 steel at 1100° F (after Soloman and Coffin, ref.38).

temperature fatigue, the frequency and environment are extremely important. At high frequencies, no effect of frequency and environment may be observed as the time at load per cycle will be insufficient for time dependent creep and corrosion processes to occur. As the frequency decreases, both environment and frequency become very important as the time at load per cycle becomes sufficient for creep and corrosion to occur with the creep properties controlling the behavior as very low frequencies are reached.

FATIGUE

The engineering use for fatigue data is to predict the life of structural components subjected to cyclic loading. This fatigue life may be divided into three continuous stages: 1)fatigue-crack initiation, 2) fatigue-crack propagation, and 3) fracture. The fracture stage, while not constituting a significant portion of the fatigue life, does limit the extent of stable fatigue-crack growth. The onset of fracture begins when a critical crack length is reached. This critical point is determined by the fracture toughness of the material, the geometry of the structure and the crack, and the applied stress. The major portion of the fatigue life of a component will be the sum of the initiation and propagation stages.

The fatigue life of components that are similar to smooth tensile bars may be controlled by fatigue-crack initiation or propagation depending on the applied stress fluctuation . This is shown schematically in Fig. 8 which is a generalized plot of total life, initiation life, and propagation life as a function of applied stress amplitude. At high stresses initiation life is negligible; but at low stresses initiation controls the life of the part. In more general circumstances, the magnitude of the initiation

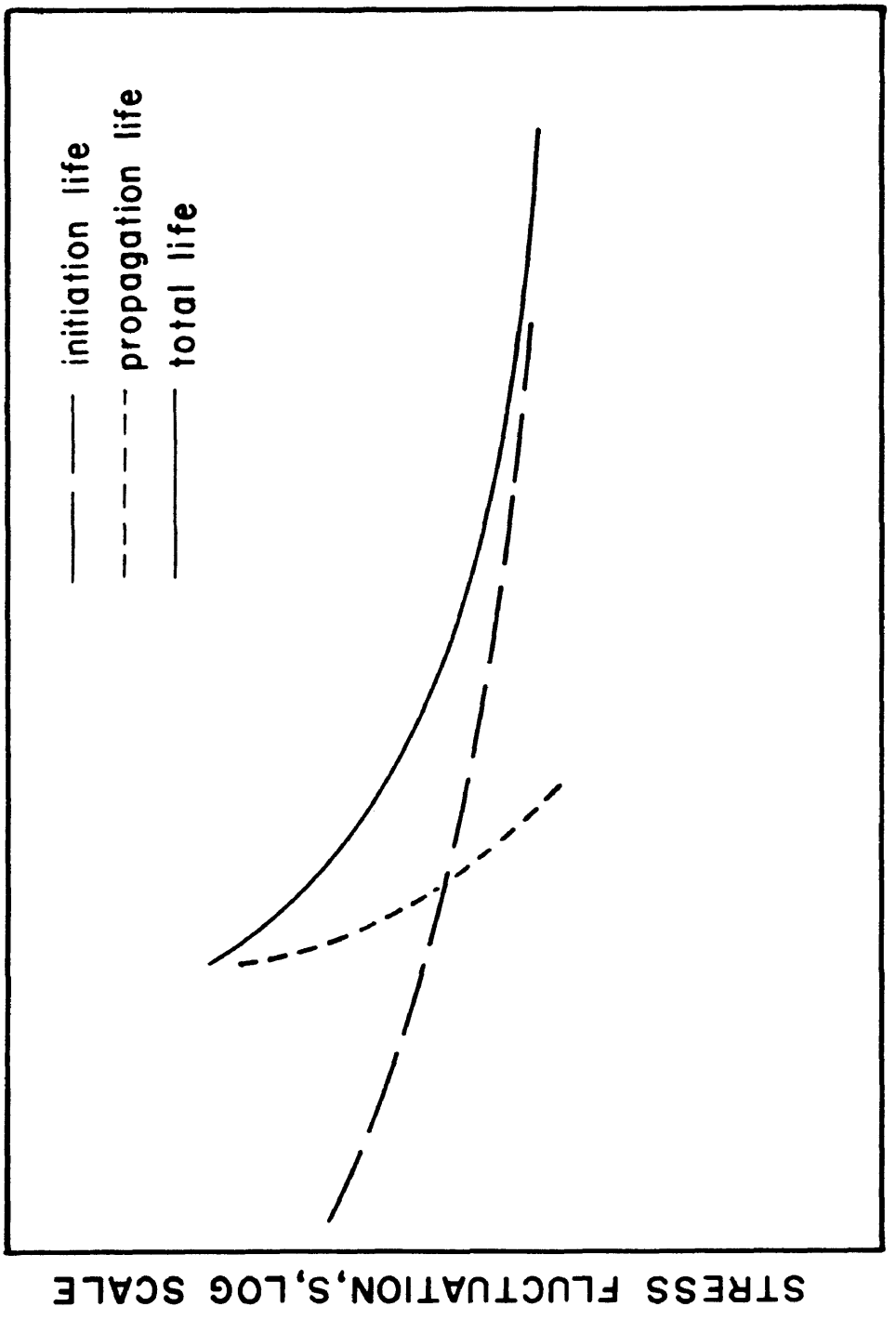

Figure 8. A typical stress fluctuation versus number of cycles to failure (S-N) curve showing the initiation and propagation portions of the fatigue life as well as the total life (after Rolfe and Barsom, ref.41).

portion of the fatigue life will depend on parameters such as stress concentrations, defects, and surface finish. Furthermore, in the safe design of most large structures, some cracks (eg. welding defects) must be assumed to exist. The fatigue life of such structures will be determined by the rate of fatigue-crack propagation. Laboratory data presented as number of cycles to failure as a function of applied stress fluctuation (S-N curves such as presented in Fig. 8) do not provide the necessary data for safe life predictions under general circumstances. For this investigation, the fatigue-crack propagation rate will be studied as it lends itself to a more rigorous analysis, and it can be analyzed without the need to distinguish between initiation, propagation, and fracture as measured in S-N type tests.

It has become generally accepted that stable fatigue-crack propagation rates can be described by the relationship proposed by Paris (39):

$$da/dN=A\Delta K^{n} \qquad [7]$$

where da/dN is the crack growth per cycle, ΔK is the stress-intensity range, and A and n are constants which may be functions of material, temperature, frequency, and environment. Because the stress-intensity factor describes the stress state at a crack tip, Equation [7] states that

the crack-growth rate is a function of the stress fluctuation at the crack tip.

The stress-intensity factors for several simple geometries which can approximate many real structures have been determined (40). Approximating the applied ΔK for a given component and assuming an initial crack size allows the life of the component to be predicted if the constants A and n are known for the appropriate conditions. The initial crack size may be assumed to be that which is the smallest detectable flaw size for the inspection procedures used and the critical crack length can be calculated from the fracture toughness of the material.

Crack growth data expressed as da/dN vs ΔK can be obtained from two basic methods. The average crack growth rate for a measurable increment of growth can be measured and recorded as a function of the average applied ΔK or the crack length can be measured periodically during a test and plotted as a function of the total number of cycles. The slope of this curve at a given crack length (applied ΔK) is the crack growth rate da/dN. The latter approach allows steady-state growth rates to be determined at many values of ΔK during a single test.

Empirical Observations and Models

Crack growth rates for metals can be divided into three regions as a function of ΔK (41) as illustrated in the schematic plot of da/dN vs ΔK for typical metals shown in Fig. 9. In Region I the values of ΔK are near the lowest value required to propagate a fatigue crack. Region III occurs in the ΔK range in which the maximum applied K approaches the critical K and unstable crack propagation begins. Region II is the region of stable fatigue-crack propagation described by Equation [7].

Within a given alloy system, especially martensitic steels, the mechanical and metallurgical properties of a material have little effect on the rate of fatigue-crack propagation in Region II as summarized by Rolfe and Barsom (41). Crack growth rates for a variety of ferrite-pearlite steels and for austenitic stainless steels show similar behavior. Similar, although more scattered, results for aluminum and titanium alloys indicate that the stable crack growth rate is not a pertinent factor for material selection within a given metal system operating in a benign environment.

Many analytical models describing the rate of fatigue crack propagation have been developed and have been reviewed in several publications (42,43). Although most of

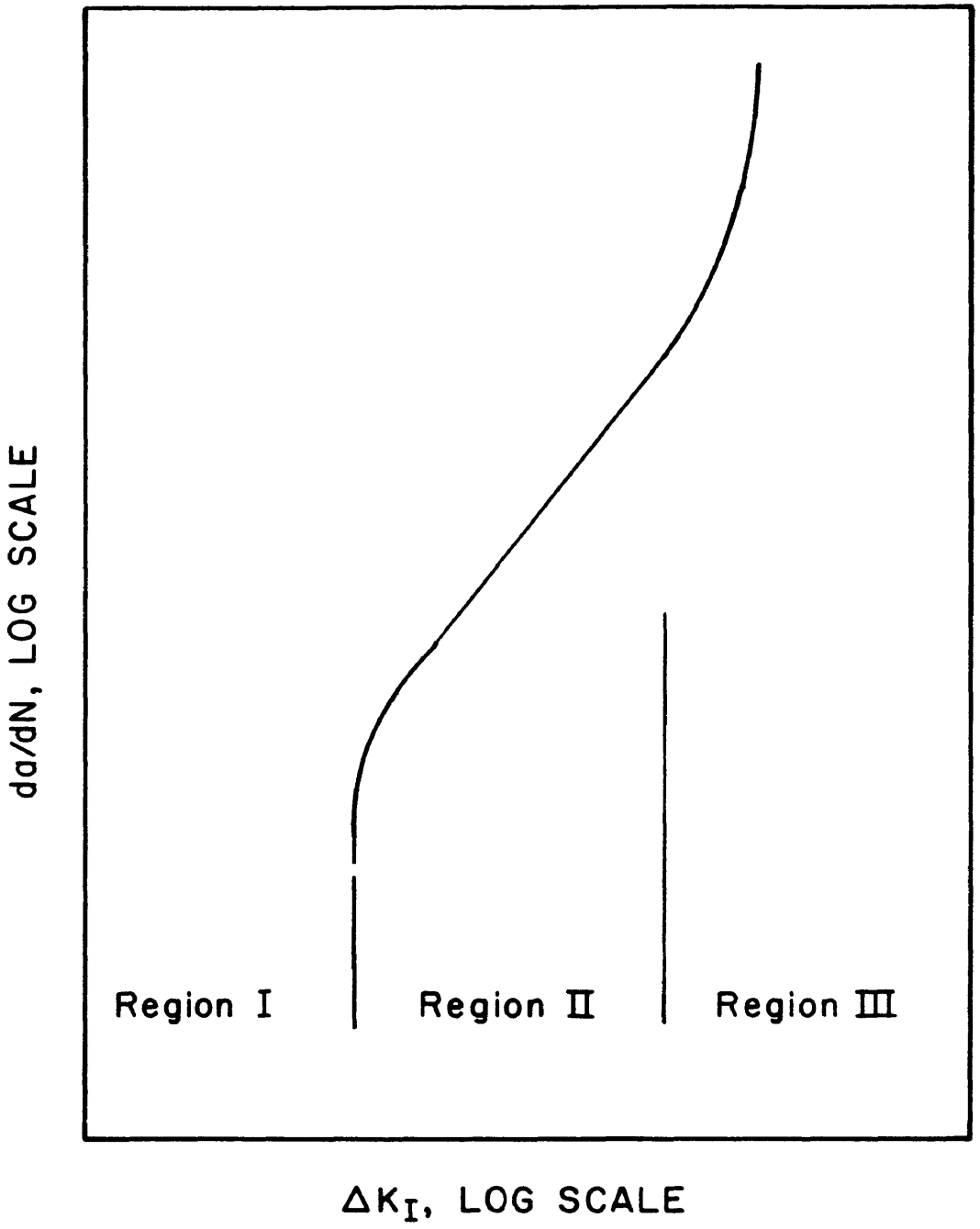

Figure 9. Crack growth rate, da/dN, as a function of stress-intensity-factor range, ΔK , for typical materials illustrating the three regions of behavior (after Rolfe and Barsom, ref.41).

these models are developed with crack length and stress as the controlling parameters, they can generally be reduced to Equation [7]. As shown by Walton and Ellison (42), many models may be expressed as

$$da/dN = C\sigma^m a^p \qquad [8]$$

where m is often equal to twice p. With K being proportional to $\sigma a^{1/2}$, Equation [7] follows.

Irving and McCartney (43) have reviewed many models and conclude that they can be divided into two groups. Models based on the instantaneous value of crack opening displacement have a stress-intensity exponent (Equation [7]) equal to 2. The second type of model is based on damage or strain accumulation and results in n=4. Although each of the models fits a limited amount of data, Paris and Erdogan (39), and Irving and McCartney conclude that for fatigue crack propagation in inert environments an exponent of 4 provides better agreement for large amounts of data. A crack growth law proposed by Irving and McCartney which is based on an energy balance within the crack tip process zone predicts n values between 2 and 4. If the zone in which the fracture process is occurring is smaller than the plastic zone but larger than the reversed plastic zone the stress exponent is equal to 4. The stress exponent is equal to 2 if the fracture process zone is contained wholly

within both the plastic and reversed plastic zones. A critical analysis of models is very difficult because only a limited amount of data in truly inert environments is available.

Of the laws reviewed by Irving McCartney (43), none considered specifically how to introduce the effects of an aggressive environment. It might be possible however, to account for environment in the particular criterion for propagation which has been assumed for the model. For example, the environment might alter the critical crack opening displacement or the critical amount of accumulated strain. The material properties at the crack tip may also be locally effected as discussed by Kamdar (32) in reference to LME. The effective fracture energy used in the approach of Irving and McCartney (43) may be assumed to be an environment sensitive parameter.

One procedure to analytically account for environment is to add an empirical time dependent crack growth term to the cycle dependent growth term for an inert environment. This results in the following equation:

$$da/dN(\text{environment}) = da/dN(\text{inert}) + (da/dt \times dt/dN).$$

The basis for this approach is the assumption that a corrosion process adds an increment of crack growth to the mechanical crack growth. It is doubtful that unstressed

corrosion rates could ever be substituted directly for da/dt but crack growth rates from stress-corrosion cracking might be useful.

At this time no theoretical model which quantitatively describes the influence of environment on fatigue crack propagation has been developed. In fact, the large number of possible environmental interactions may make it impossible to account for all of them in one model. It appears that a better understanding of fatigue crack propagation in an inert environment is necessary before the complex effects of environmental interacton can be successfully modeled.

INTRODUCTION SUMMARY

This literature review, although far from complete, has shown stress/environment interactions to be very complex. The nature of such interactions ranges from general corrosion to enhanced local corrosion at the tip of a crack to the effect of an atom from the environment on the electronic bond between individual atoms in the material. The degradation of material properties due to the environment is most pronounced at the tip of a crack whether the interaction is due to stress-corrosion cracking, corrosion fatigue, liquid-metal embrittlement, or a high-temperature fatigue phenomena. Therefore, in order to study stress/liquid-lithium interactions, this investigation will impose the most severe conditions: Fatigue-crack propagation in which the cyclically stressed material at the tip of a crack will be exposed to liquid lithium. With the crack extensions occurring during a single cycle being very small (ie. 10^{-7}m), the rate and mode of fatigue crack propagation should be very sensitive to the effects of the molten lithium environment.

EXPERIMENTAL PROCEDURE

This test program consists of two parts; fatigue testing and metallography. Precracked, fracture-mechanics specimens were used for fatigue testing so that the data could be analyzed according to Equation [7] (from the Introduction). Fatigue tests were performed in a liquid-lithium environment and in argon at several frequencies. One half of each specimen was used for scanning-electron microscopic examination and one half for optical metallography. The purpose of the microscopic examination was to determine the mode of crack propagation in each environment.

Equipment

A Model 810 Material Test System was used for fatigue testing in this study. This system includes an MTS 10

metric ton load frame, a 6 gpm (at 3000 psi) hydraulic power supply, and appropriate electronic controls. A function generator supplied a control sine wave for fatigue testing and a ramp function for compliance measurements (to be discussed later). A digital voltmeter with peak monitoring capabilities allowed the maximum and minimum values of the applied sinusoidal load function to be monitored. During fatigue testing, this feature allowed the system to be adjusted to give the desired load range at high frequencies (greater than 10 Hz) where the nominal set point and span settings are not valid.

The standard upright load frame was adapted to a protective atmosphere glove box. This box was necessary because lithium is highly reactive and reacts readily with oxygen, nitrogen, and water. Adaptation was facilitated by placing the actuator in the upper crosshead of the load frame.

The argon atmosphere in the glove box was purified by a VAC Atmospheres MO-40-1V Dri-Train (to remove oxygen and water). The NI-20 Ni-Train (for nitrogen removal), which is in series with the Dri-Train, was not used for these tests. The box atmosphere concentration of 200-300 ppm oxygen and 1400-2000 ppm nitrogen produced a nitrogen concentration of approximately 2000 ppm in the lithium.

The test fixturing was designed for testing in an open crucible mounted in the glove box, with or without liquid lithium. Figure 10 is a cutaway drawing of a crucible with a compact tension specimen mounted in the upper and lower grips with pins. The horizontal slot in the lower grip allows the pin to slide in sideways making it possible to insert or remove specimens with the upper grip rod while the crucible is filled with molten lithium. Because of this feature, tests could be performed consecutively without long delay times and without removing the lithium from the crucible. The crucible and the grips were made of 304L stainless steel to avoid dissimilar metal effects with the specimens.

The lower grip threads into the bottom of the crucible which is held rigidly by a threaded rod connecting the crucible to a plate which is bolted through the box to the lower platen of the load frame. The load is transmitted from the actuator (mounted in the upper crosshead) to the specimen by the upper grip rod which is connected to the load cell through a U-joint. This load train enters the protective atmosphere box through a rubber bellows. The photograph in Fig. 11 shows the upper grip rod, furnace, and crucible as well as the extensometer which is used to measure the displacement between the upper grip rod and the

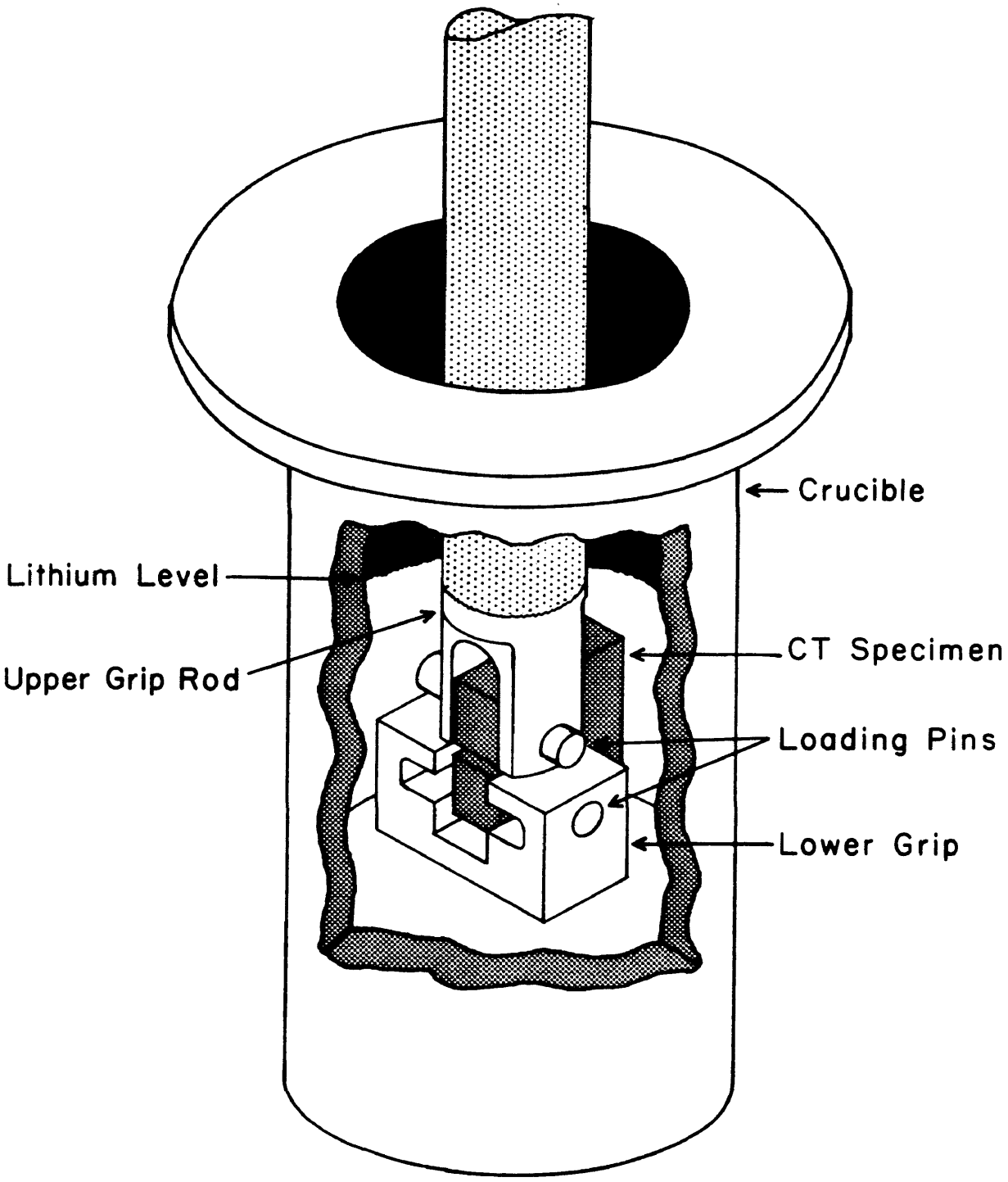

Figure 10. A cutaway drawing of the test fixturing used in this investigation which shows a CT specimen mounted in the upper and lower grips.

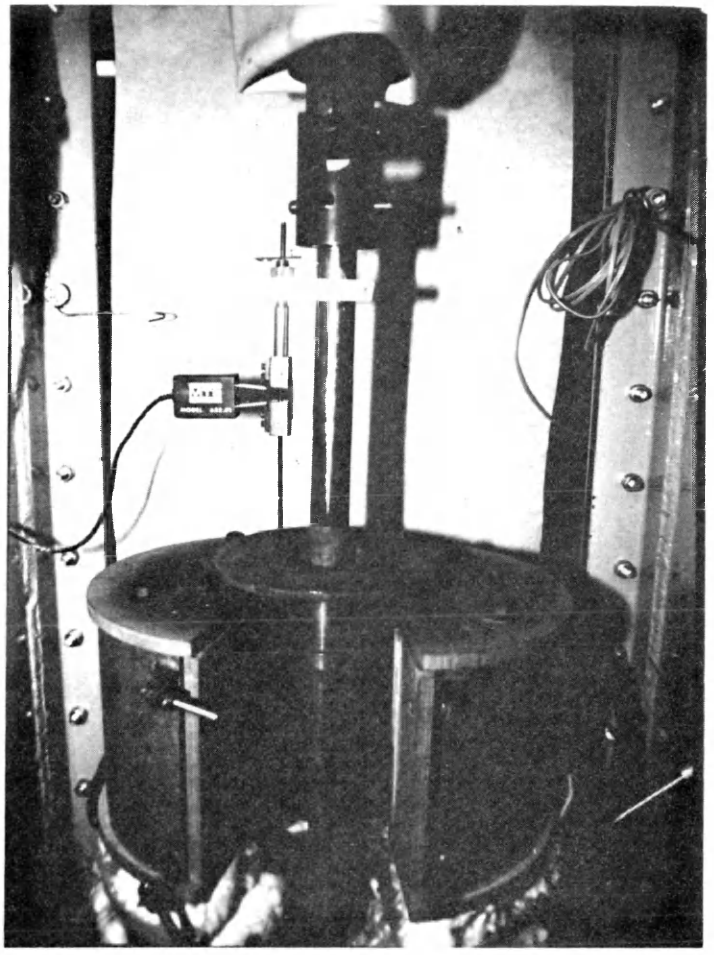

Figure 11. A photograph of test fixturing in the protective atmosphere box showing the furnace, upper grip rod, and crucible as well as the extensometer and bracket used for measuring compliance.

crucible. This displacement was used to determine the specimen compliance as will be discussed later under Techniques.

Compact tension (CT) specimens were selected for this investigation for several reasons. The stress-intensity factor, K_I, for the CT geometry is accurately calibrated as a function of applied load, crack length, and specimen dimensions, and thus, the data obtained can be used in a fracture mechanics approach to design as indicated in the Introduction. The equation for K_I is included in Fig. 12 which is a line drawing of the CT specimens used in this investigation. The specimens were machined from 304L stainless steel plate (1/2 inch thick) to ASTM Standard E399 with the width, W, equal to one inch. The crack propagation direction was perpendicular to the rolling direction and the rolling plane. The small specimen size allowed small volumes of lithium to be used and, because of the low loads necessary, lighter fixturing could be used when compared to larger specimens.

Techniques

In order to obtain crack-growth-rate data, the crack length has to be measured periodically during fatigue cycling. Because testing was performed in a protective

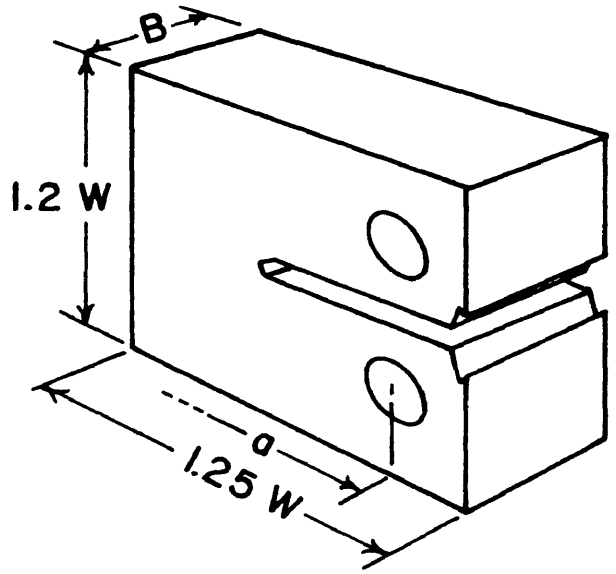

$$K = \frac{P\,a^{1/2}}{B\,W}\left[\,29.6 - 185.5\left(\frac{a}{W}\right) + 655.7\left(\frac{a}{W}\right)^2 - 1017.0\left(\frac{a}{W}\right)^3 + 638.9\left(\frac{a}{W}\right)^4\,\right]$$

a = crack length
B = 12.7 mm
P = load
W = 25.4 mm

Figure 12. A line drawing of the CT specimens used in this investigation. The K-calibration function is also presented.

atmosphere box at high temperatures with the specimens submerged in molten lithium, a remote technique for crack length measurement was needed. In this investigation, a technique described by McHenry (44) was used.

McHenry (44) has shown that crack lengths in CT specimens can be found from compliance measurements where compliance is the inverse slope of a load-deflection curve. The deflection used by McHenry was the separation of the crack faces at a point beyond the load line. A continuous recording of load and deflection as the load is increased from the minimum to the maximum fatigue values yields a straight line. McHenry used a simple extension of concentric tubes to translate the displacement out of a furnace so that the compliance could be measured when testing at high temperatures. The crack length is found by comparing the measured compliance to a previously determined compliance calibration curve.

McHenry (44) determined the compliance calibration curve by measuring the compliance of CT specimens as a function of known crack lengths. The known crack lengths were produced by propagating a fatigue crack at a given load range and then increasing or decreasing the load range. The differences in growth rates and plastic zone sizes change the texture of the surface leaving a band for

each change in load range. An example of a fracture surface from this investigation, with a distinct band for each load range, is shown in Fig. 13. Because the crack front is not necessarily straight (refer to Fig. 13) an average value of crack length was used. McHenry used the average of the 1/4 and 3/4 thickness values which was the value used in this investigation. McHenry normalized the compliance curve for specimen size, temperature, and material by multiplying the compliance by the elastic modulus and specimen thickness and by dividing the crack length by the specimen width.

Due to anticipated problems arising from testing in liquid lithium, a modified compliance was used in this investigation. Capillarity of liquid lithium in concentric tubes such as those used by McHenry (these tubes were part of the simple extension used when testing at elevated temperatures) required that a different method of measuring the sample deflection be established. The extensometer, bracket, and rod shown in Fig. 11 were used to measure the displacement between the crucible and upper grip rod. This displacement includes bending of the loading pins, deflection in the grips, and the desired specimen deflection. Using the total displacement, a modified system compliance was measured. The resulting calibration

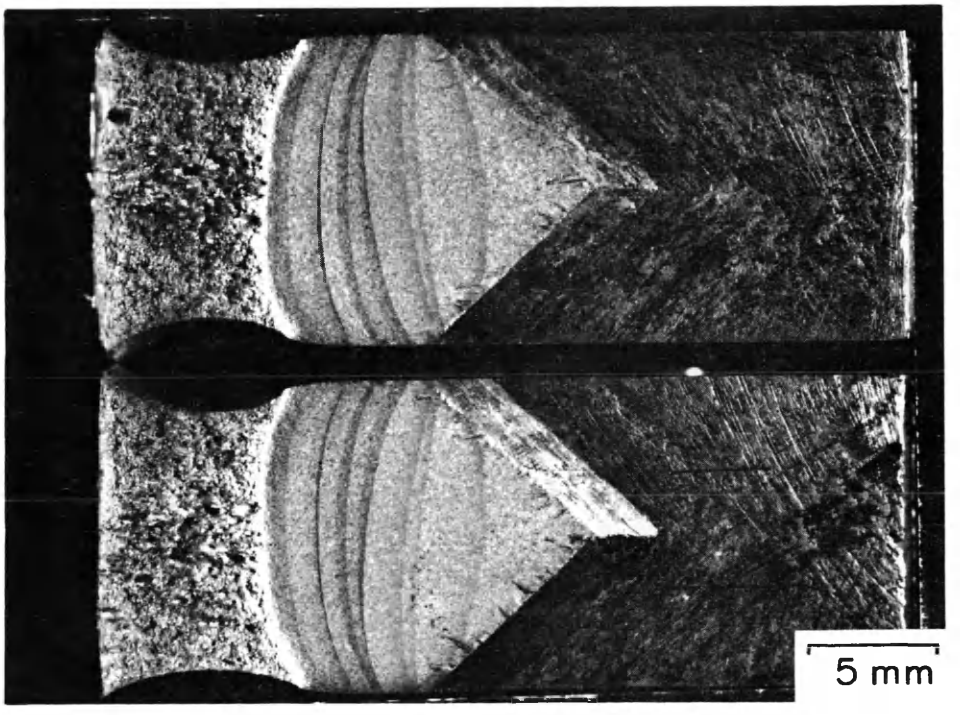

Figure 13. A fractograph of a compliance calibration specimen illustrating the banding produced by periodic changes in the load amplitude.

curve is shown in Fig. 14. This technique is valid because all of the fixturing which contributes to the measured compliance remains unchanged, so the system compliance varies only with crack length as in the technique described by McHenry (44). The load-deflection curve measured in this way was observed to be non-linear due to deflections of the grips and loading pins. As shown in Fig. 14, defining the compliance at a particular load (ie. 300 lb) allowed a consistant correlation between compliance and crack length to be made. Figures 13 and 14 show that the modified system compliance can be used to determine crack lengths.

In this investigation, one compliance calibration curve was determined at room temperature. The elevated temperature readings were multiplied by a constant determined from the measured and expected compliances for the initial and final crack lengths (measured after the test was completed). This procedure was used because the temperature dependence of the compliance is reported to be due entirely to the elastic modulus (44). Values of the elastic modulus for austenitic stainless steel at room temperature and at 1200 F (649 C) (45) give a ratio of moduli equal to 0.75. This value is similar to the values for the constant (0.68 to 0.86) for this investigation.

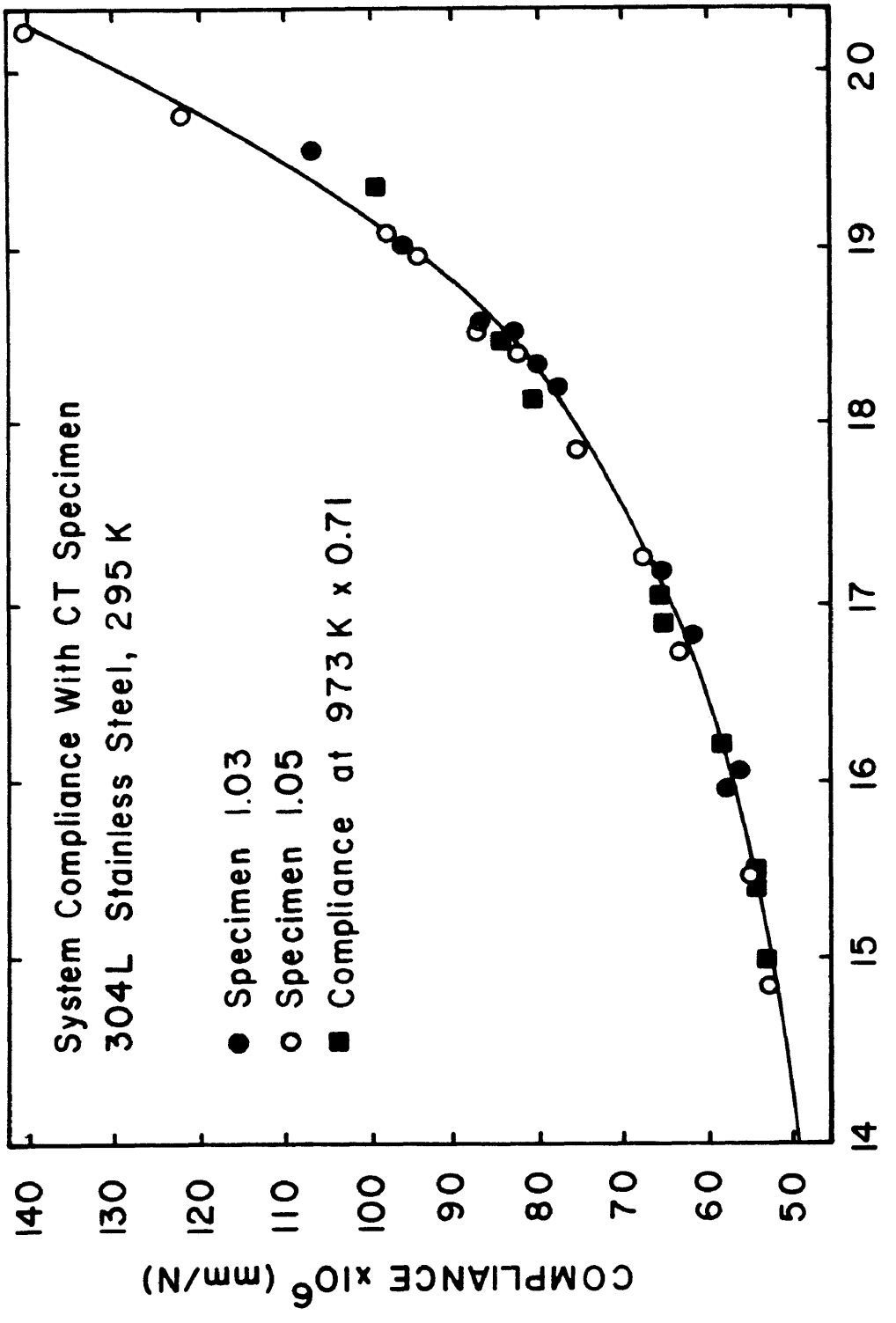

Figure 14. The modified, system-compliance-calibration curve used to determine crack lengths. This curve, which is for room temperature at a load of 3001b (1980N), includes two room temperature calibration specimens and one 973 K specimen corrected for temperature.

The variation in these constants, which can be found in the Appendix, was attributed to variations in the bending of the grips and loading pins. Temperature corrected compliances from a high-temperature-calibration specimen, plotted in Fig. 14, show this procedure to be valid.

The temperature corrected compliances were converted to crack lengths (see the Appendix) and plotted against the number of fatigue cycles as shown in Fig. 15 which is an a vs. N plot. Crack growth rates (da/dN) were then measured graphically and plotted as a function of stress-intensity range, calculated for the given crack length and load range according to the equation presented in Fig. 12. The stress-intensity range is plotted on the axis opposite crack length in Fig. 15.

Before testing, the CT specimens were surface ground to 600 grit and then vacuum heat treated for 2.5 hr at 1173K which resulted in a microstructure of equiaxed grains 50μ in diameter. The specimens were then fatigue precracked at room temperature to provide a constant initial test condition of a sharp fatigue crack about 0.55 in. long measured from the center of the loading pins.

Samples were submerged in liquid lithium for 24 hours prior to loading to allow the temperature and concentrations of dissolved elements in the lithium to

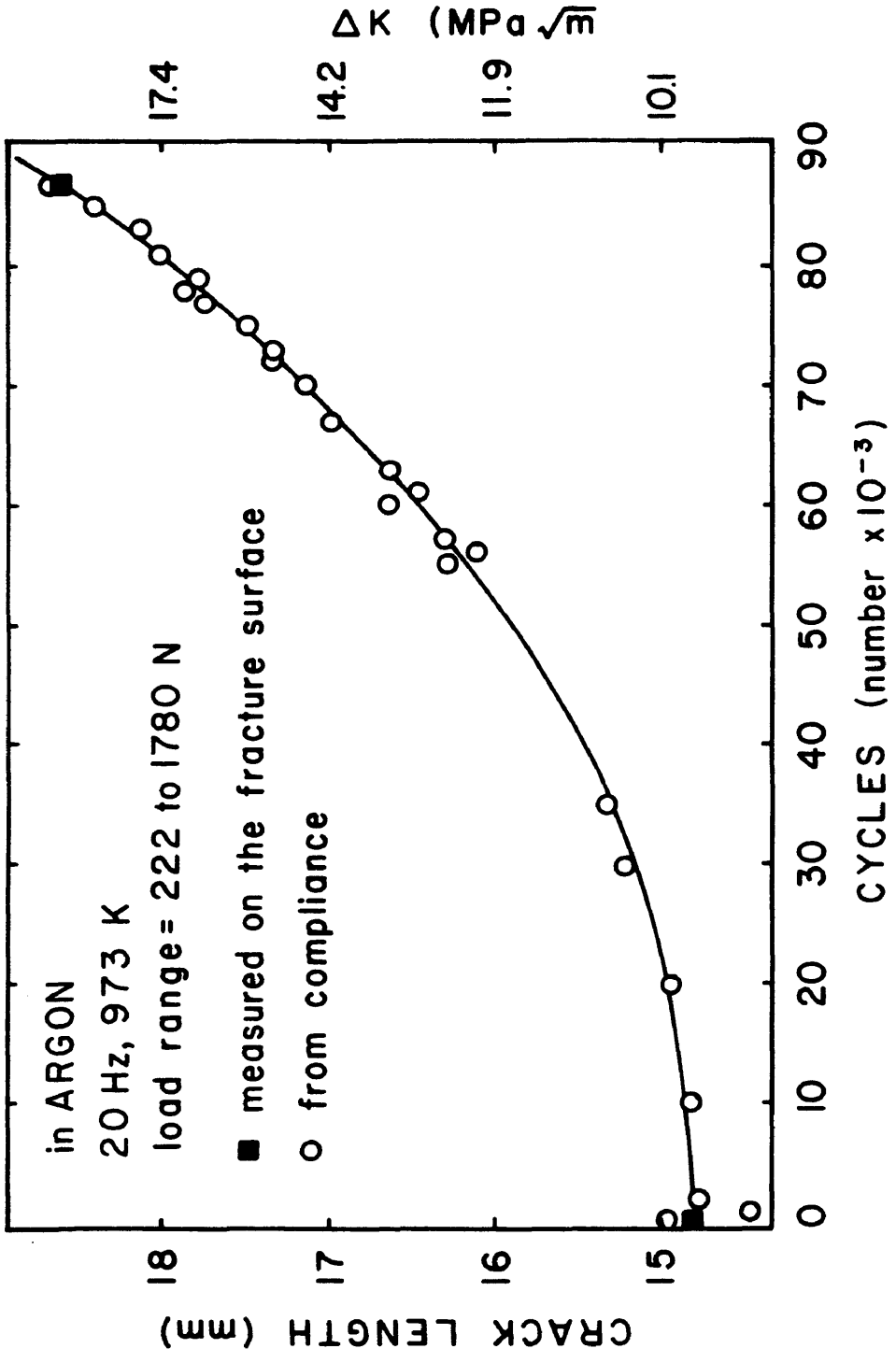

Figure 15. Crack length and calculated stress-intensity-factor range as a function of number of cycles (a vs N) for the specimen tested in argon at 20 Hz.

reach a quasi-steady state. The samples were then fatigue cycled using a sinusoidal load cycle. Compliance was measured using a linear loading cycle up to the peak load experienced during fatigue cycling. This was measured at intervals of about 0.010 in. of crack growth.

Tests were terminated before failure to facilitate removal and for metallography. Each sample was sectioned perpendicular to the crack plane so that optical metallography of the crack tip could be performed on one half. The other half was fatigue cycled to failure at room temperature in air. The exposed fracture surfaces were then examined in a scanning electron microscope.

A micro-Kjeldahl technique was used to determine the nitrogen content in the lithium. This technique has been used in several investigations and is described by Schlager et al (46). Samples of the molten lithium were drawn into a 1/4 in. diameter stainless steel tube. The bottom 2 in. of the samples were discarded with the next 2 in. analyzed for nitrogen content. This left an additional 2 in. at the top which was also discarded.

RESULTS AND DISCUSSION

The crack growth rates are presented as straight lines on plots of log crack growth rate (da/dN) versus log stress intensity range (ΔK), according to equation [7]. These growth rates were derived from the data presented in the Appendix plotted as a vs. N. The growth rates in argon and in lithium are compared in Figure 16 (20 Hz), Fig. 17 (1.7 Hz), and Fig. 18 (0.067 Hz), each curve representing one test. The argon box atmosphere for these tests contained 200-300 ppm oxygen and 1400-2000 ppm nitrogen with the lithium containing about 2000 ppm dissolved nitrogen.

Several important observations can be made with respect to Figures 16,17, and 18. First, the crack growth rate for a given ΔK is higher when propagation occurs in a liquid-lithium environment than when it occurs in the argon environment at each frequency. The low growth rate argon

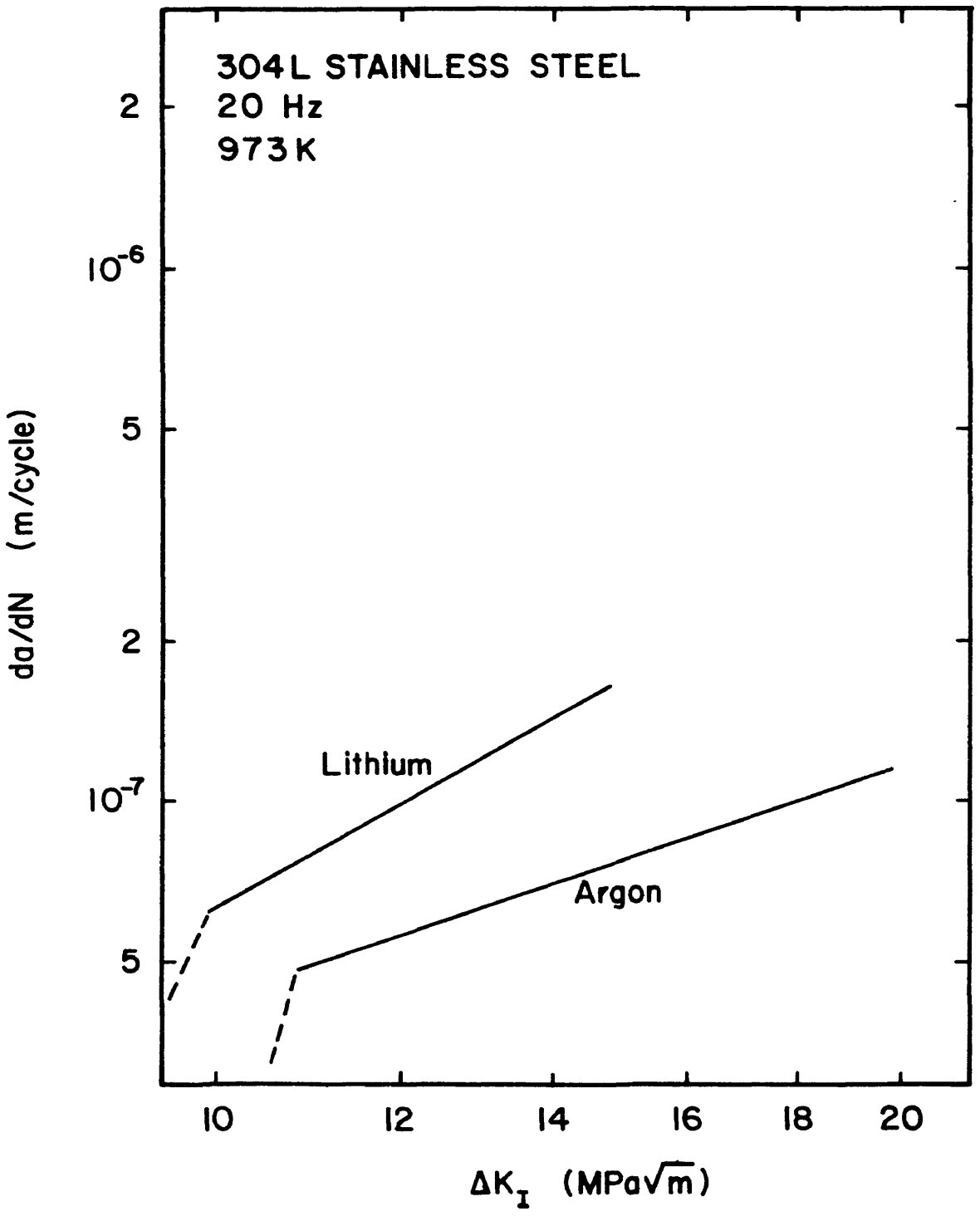

Figure 16. Crack growth rate, da/dN, as a function of stress-intensity-factor range, ΔK, for 304L stainless steel tested at 20 Hz in lithium and argon at 973K.

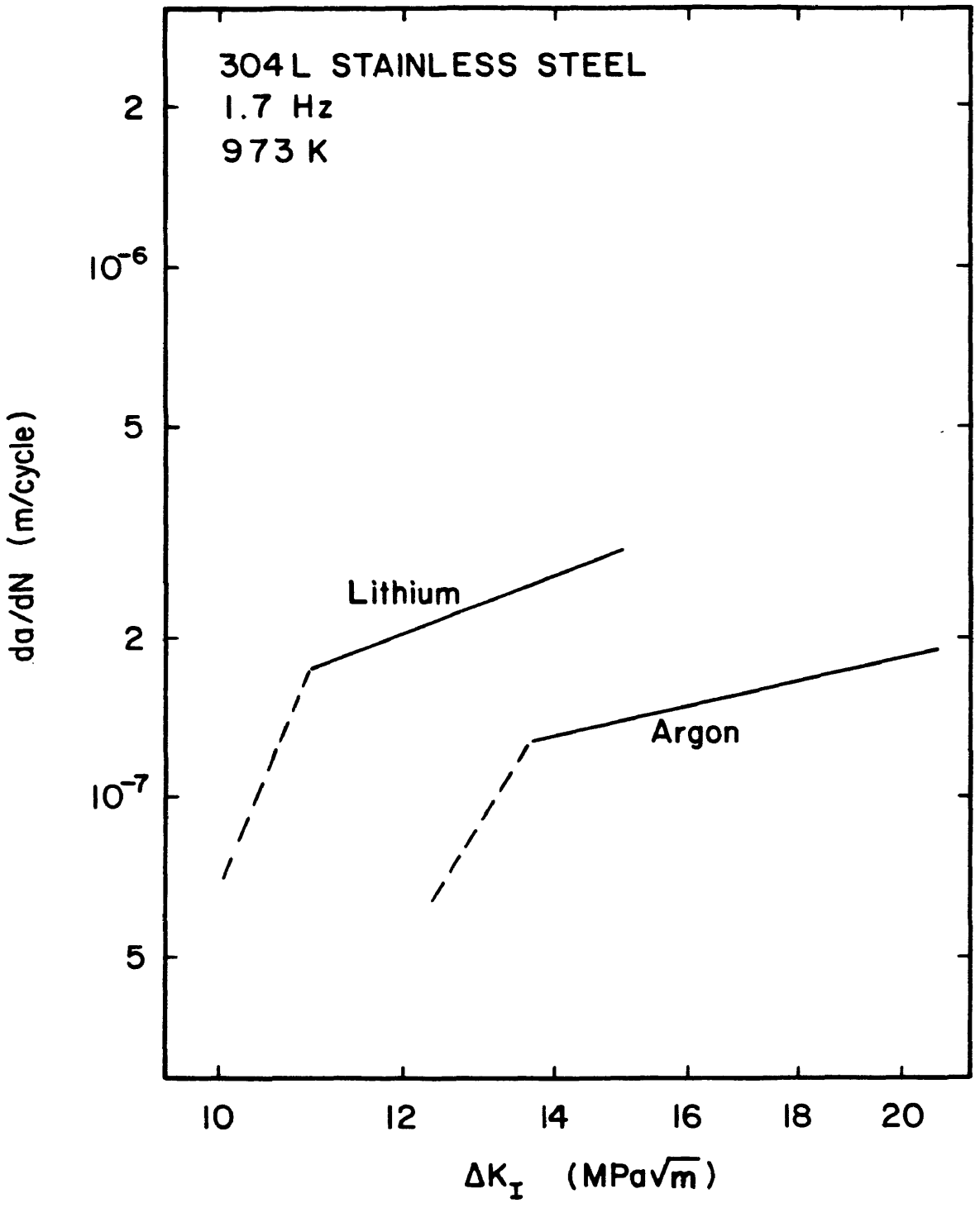

Figure 17. Crack growth rate, da/dN, as a function of stress-intensity-factor range, ΔK, for 304L stainless steel tested at 1.7 Hz in lithium and argon at 973K.

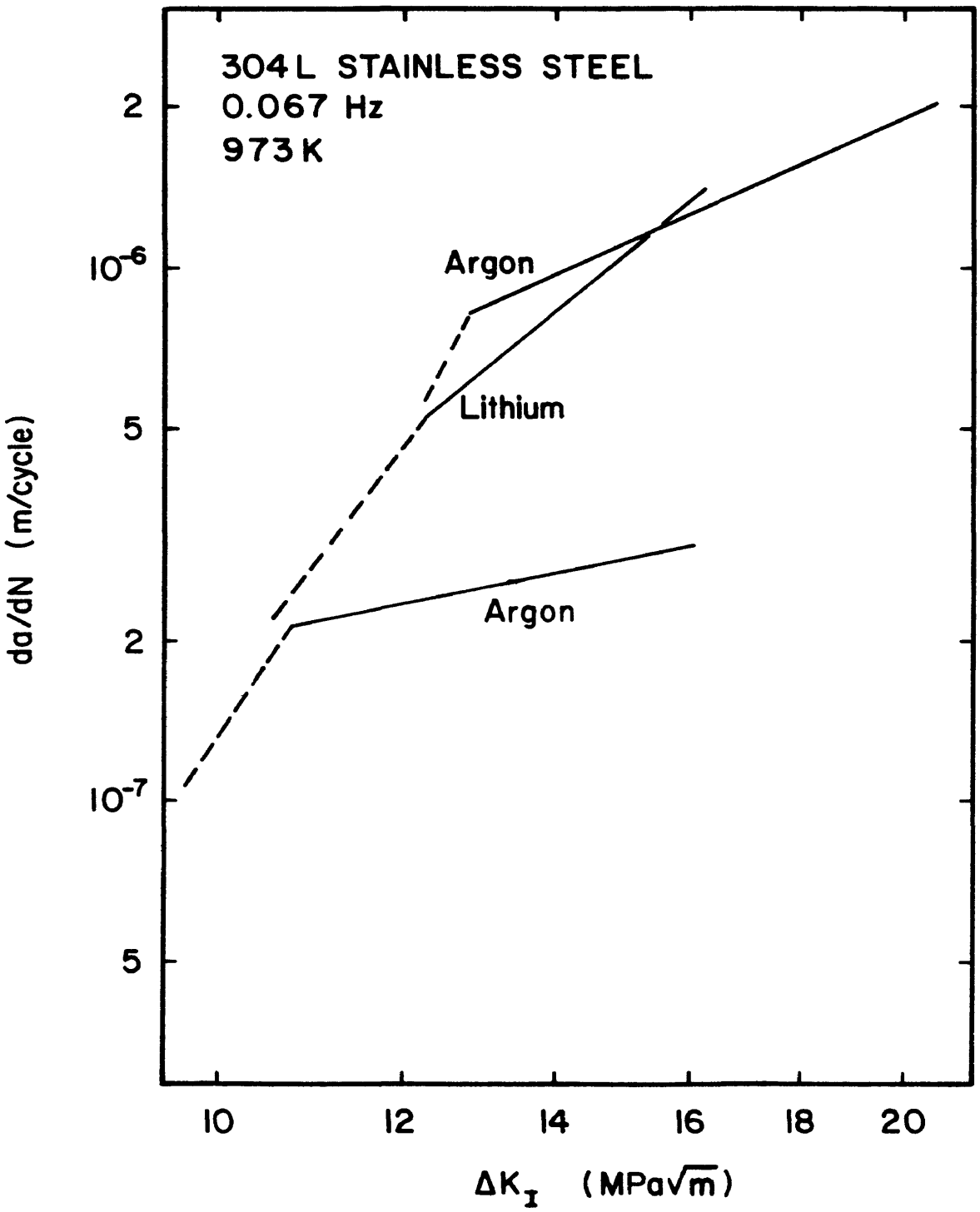

Figure 18. Crack growth rate, da/dN, as a function of stress-intensity-factor range, ΔK, for 304L stainless steel tested at 0.067 Hz in lithium and argon at 973K. The two argon curves represent two separate specimens.

curve in Fig. 18 is considered the best representation of propagation in an inert environment. The difference in growth rates for the argon tests at 0.067 Hz is attributed to a higher peak load and oxygen concentration during the high growth rate test. This will be discussed later with emphasis on the effect of oxygen partial pressure on fatigue-crack propagation.

Another important observation with respect to the influence of lithium is that for each frequency, the slope of the growth rate curve for the lithium environment is greater than that for the argon environment. This is reflected by an increase in the stress-intensity-range exponent (n in Equation [7]). Values for n and A are tabulated in Table I for each of the test conditions. A change in slope with increasing ΔK, shown by the dashed lines in Figures 16, 17, and 18, was observed in each test. However, this may be due to non-steady state conditions rather than a change in steady state propagation. The validity of this observation will be discussed further with respect to the metallographic studies.

The final observation made with respect to these figures is that for both the argon and lithium environments, the fatigue-crack-propagation rate increases with a decrease in frequency. The effect of frequency and

TABLE I

FREQUENCY (Hz)	ENVIRONMENT			
	Lithium		Argon	
	A	n	A	n
0.067	9.5×10^{-11}	3.4	7.2×10^{-9}	1.9
			2.3×10^{-8}	0.93
1.7	6.0×10^{-9}	1.4	1.5×10^{-8}	0.82
20	2.9×10^{-10}	2.3	1.7×10^{-9}	1.4

where: $da/dN = A\Delta K^n$, for da/dN in m and ΔK in $MPa\sqrt{m}$.

Table I. The constants for the equation $da/dN = A\Delta K^n$ for 304L stainless steel at frequencies of 0.067, 1.7, and 20 Hz in lithium and argon at 973 K.

environment on da/dN is summarized in Fig. 19 which plots crack growth rate as a function of frequency at a constant stress intensity range for both environments. Figure 19 emphasizes two previous observations: 1) The growth rate in lithium is greater than in argon by a factor of approximately two and 2) The growth rate increases with decreasing frequency. Because the crack growth rate in lithium increases faster than in argon with respect to stress-intensity range, the increase in growth rate due to the presence of lithium will increase with increasing stress-intensity range.

A comparison of Fig. 19 with Fig. 7 is very useful in understanding the results presented thus far. Soloman and Coffin (38) attribute the increase in crack growth rate with a decrease in frequency (Fig. 7) below the purely cycle dependent range (about 10^3 cpm) to an increase in the effects of the time dependent or creep component of crack growth. This is accompanied by a transition from transgranular propagation at high frequencies to intergranular propagation at low frequencies. The effect of the aggressive environment (air in Fig. 7) is to increase the rate of propagation and to enhance intergranular propagation at higher frequencies. The results of this investigation in the frequency range 0.067

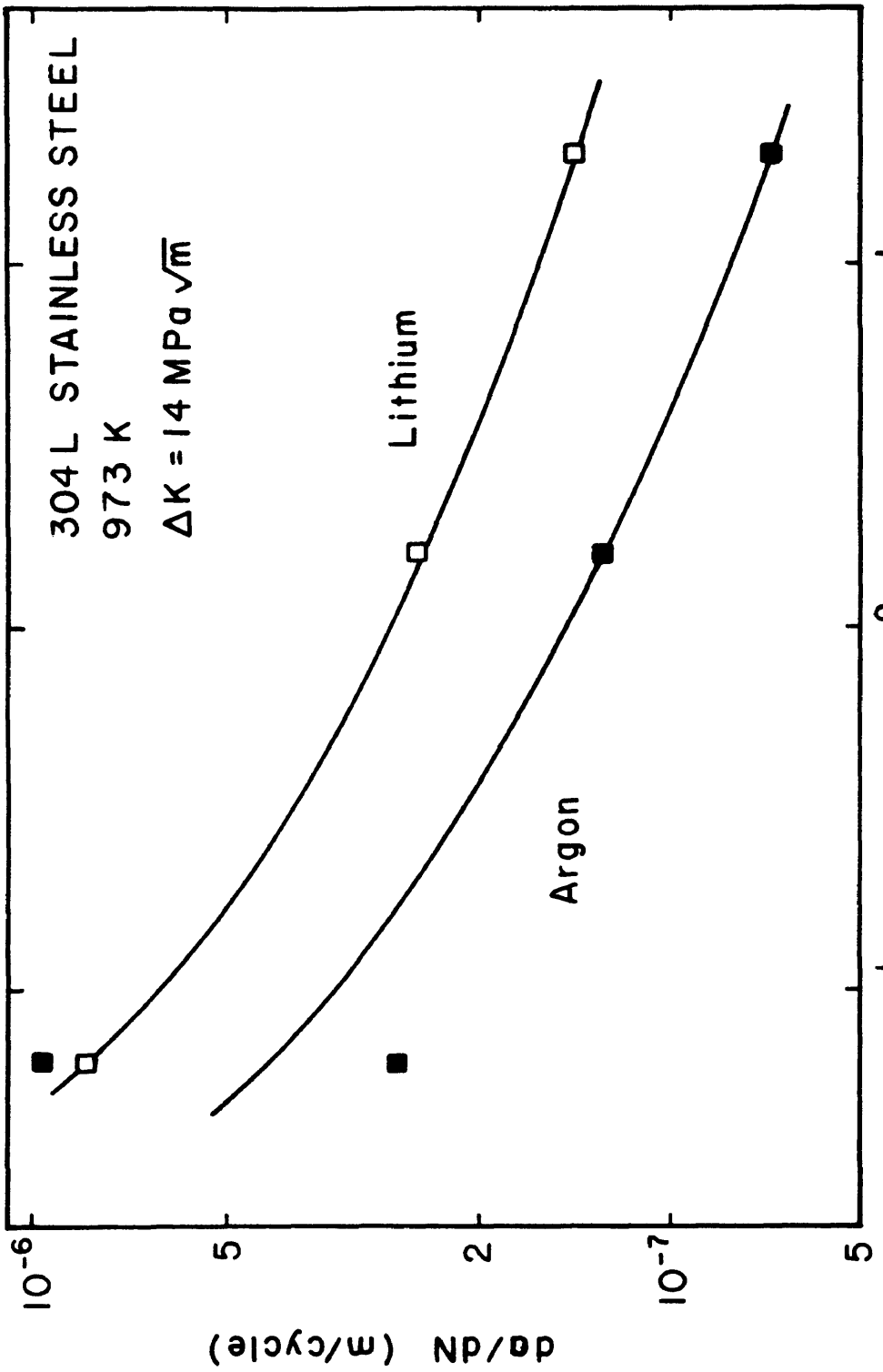

Figure 19. The effect of environment and frequency on the rate of fatigue crack propagation in 304L stainless steel at 973K and a stress-intensity range of 14 MPa$\sqrt{m}$.

to 20 Hz (Fig. 19) are very similar to the frequency range 10^{-2} to 10^{0} cpm presented in Fig. 7. The following results of a fractographic analysis are used to evaluate the effect of lithium on the mode of fatigue crack propagation in 304L stainless steel.

Figures 20, 21, and 22 are scanning electron micrographs of the fracture surfaces of samples tested in argon and in lithium at 20, 1.7, and 0.067 Hz, respectively. At 20 Hz, (Fig. 20) the sample tested in lithium exhibits a well defined intergranular fracture contrasted to the primarily transgranular fracture of the sample tested in argon. Figure 21 shows the same to be true at 1.7 Hz although some intergranular fracture is seen in the argon sample. At 0.067 Hz (Fig. 22) however, crack propagation is primarily intergranular for both samples.

The effect of frequency on the mode of crack propagation in argon can be seen by comparing Figures 20(a), 21(a), and 22(a). As the frequency is decreased, the propagation mode changes from primarily transgranular at 20 Hz to primarily intergranular at 0.067 Hz. Also, the amount of secondary cracking is seen to increase as the frequency decreases. Comparison of Figures 20(b), 21(b), and 22(b) shows the effect of frequency when testing in a lithium environment. Because crack propagation is

(a) ARGON

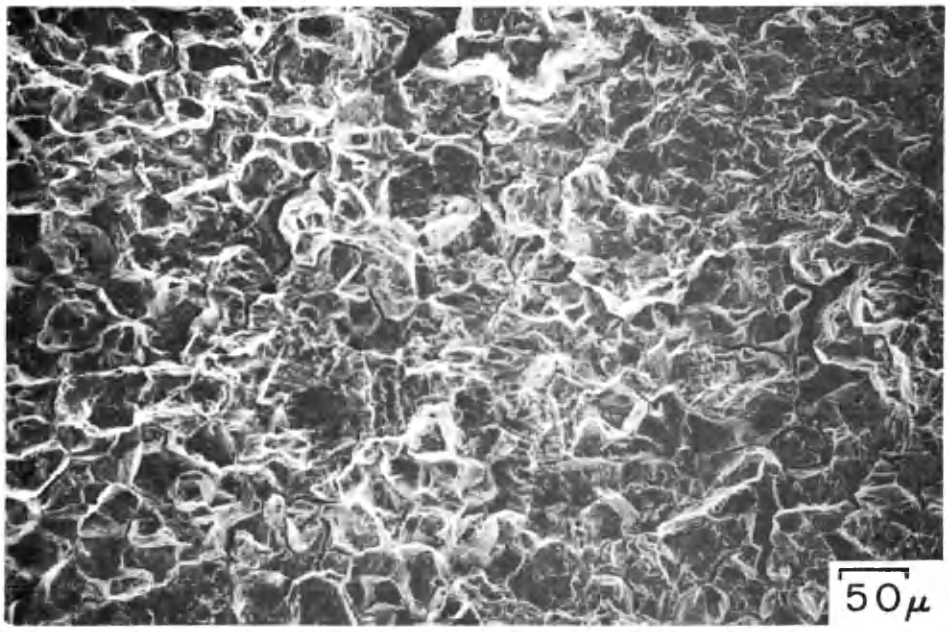

(b) LITHIUM

Figure 20. SEM fractographs of the specimens tested at 20 Hz in argon (a) and lithium (b) where ΔK was approximately 14 MPa$\sqrt{m}$.

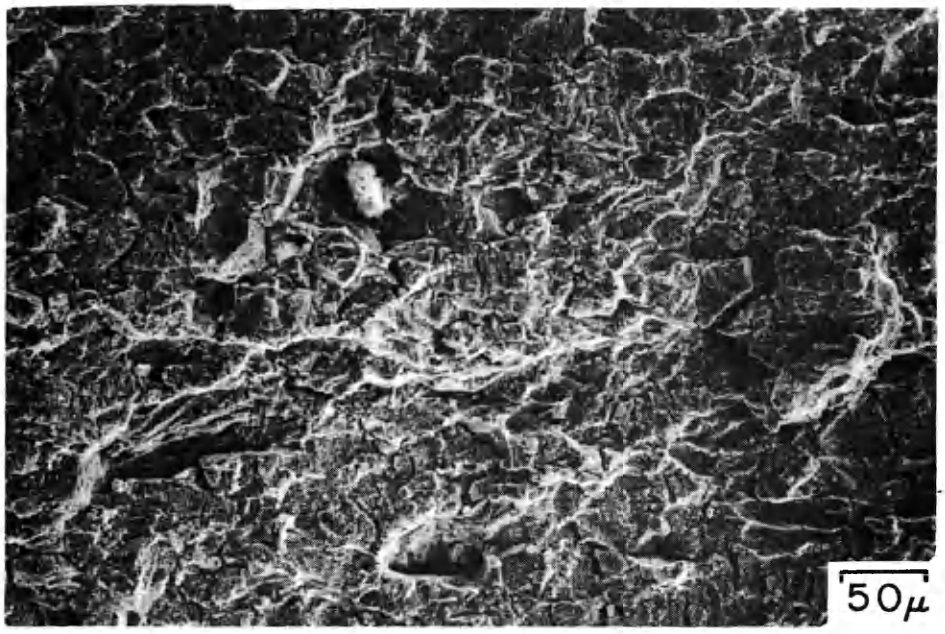

(a) ARGON

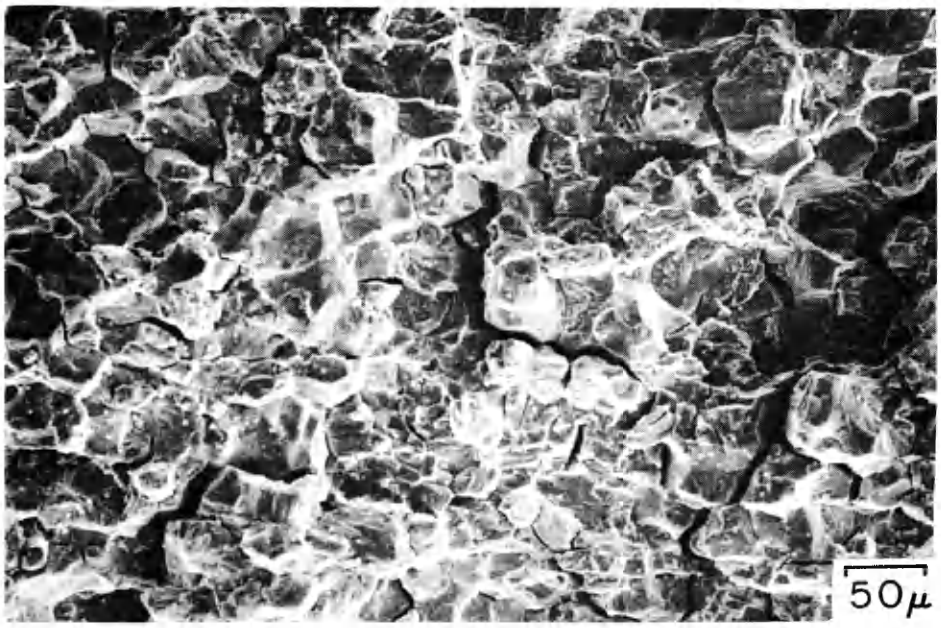

(b) LITHIUM

Figure 21. SEM fractographs of the specimens tested at 1.7 Hz in argon (a) and lithium (b) where ΔK was approximately 14 MPa$\sqrt{m}$.

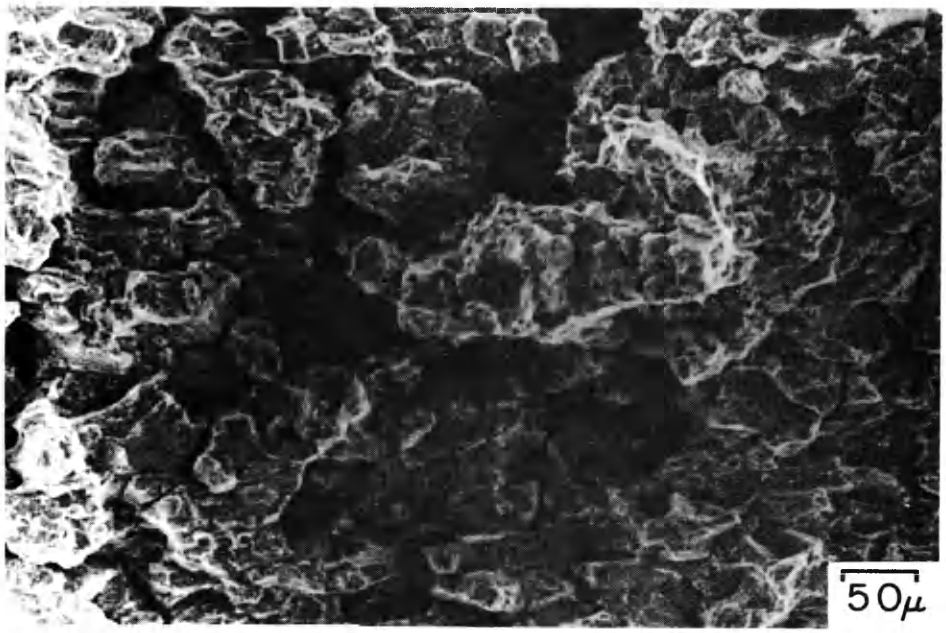

(a) ARGON

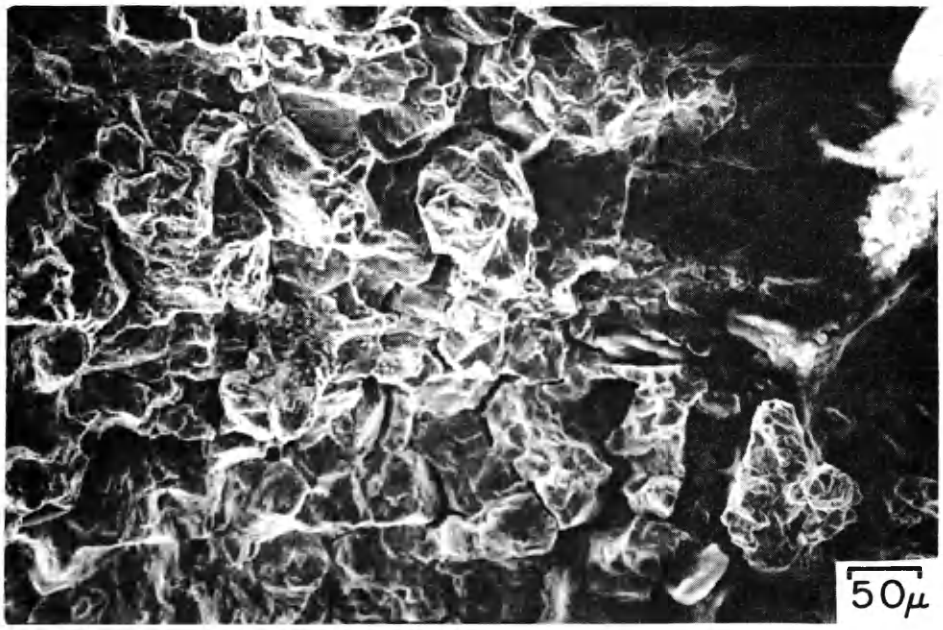

(b) LITHIUM

Figure 22. SEM fractographs of the specimens tested at 0.067 Hz in argon (a) and lithium (b) where ΔK was approximately 14 MPa$\sqrt{m}$.

intergranular, even at 20 Hz, no change in the mode of propagation is observed although the amount of secondary cracking increases as the frequency decreases similar to the phenomena observed in argon. The fractographic analysis presented here was confirmed by optical metallography of the crack tips as shown by the optical micrographs in Fig. 23. These micrographs show the intergranular fatigue-crack path at the beginning (a) and end (b) of the 1.7 Hz test in lithium.

In addition to these results, it was determined that no change in the mode of crack propagation occurred during any single test. This is shown in Fig. 23 as well as in Fig. 24 which contains scanning electron micrographs taken at the beginning and end of the high-temperature-fatigue test zone of the sample tested in lithium at 1.7 Hz. This is an important observation in light of the fact that a change in slope was observed in each of the da/dN versus ΔK curves (Figures 16, 17, and 18). This suggests that the slope change is due to non-steady state conditions at the beginning of each test rather than a change in the steady-state propagation characteristics.

The results of this metallographic examination do suggest that the effect of environment and frequency on the mode and rate of fatigue crack propagation in 304L

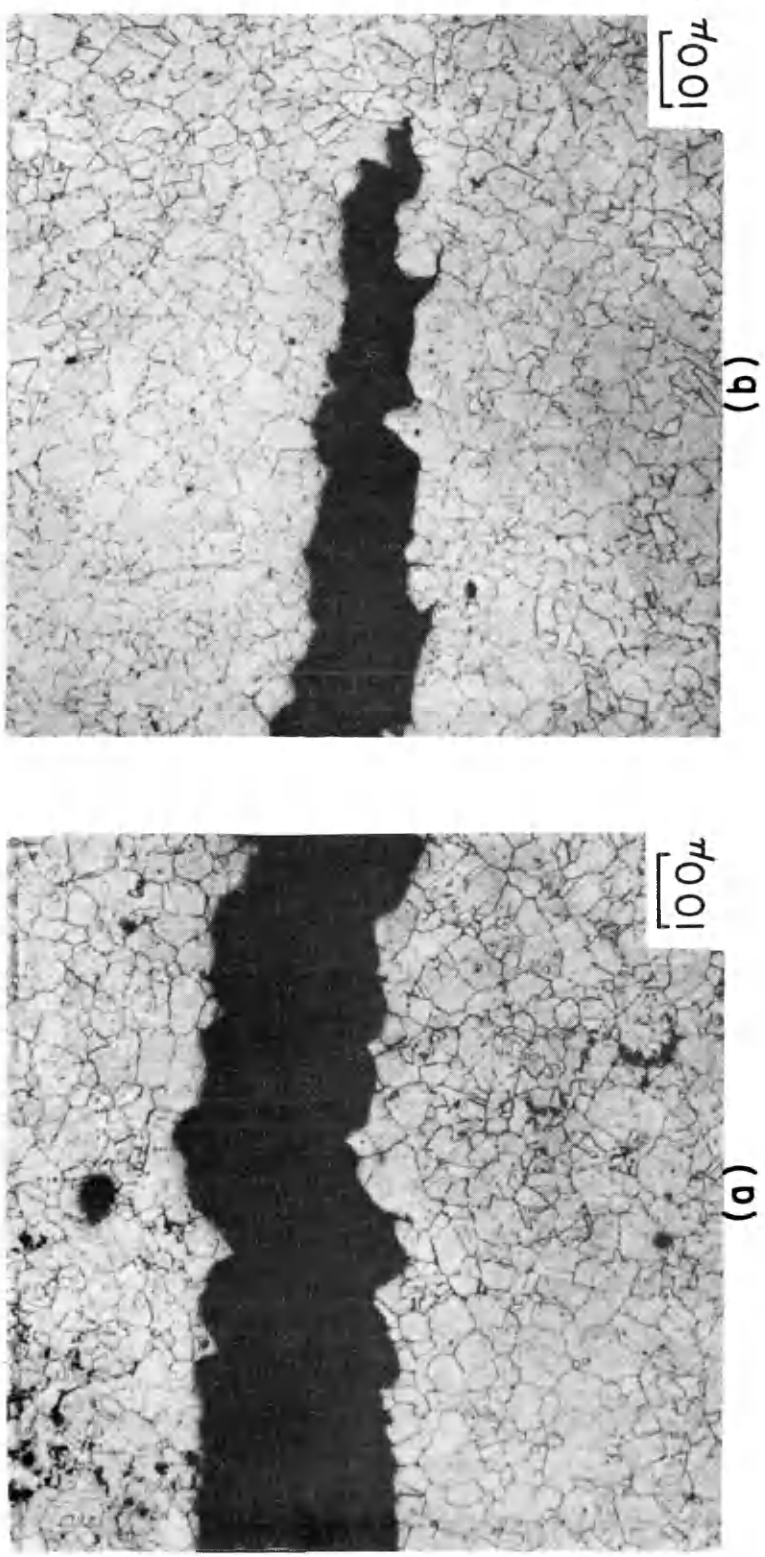

Figure 23. Optical micrographs of the beginning (a) and end (b) of the high-temperature-test zone of the specimen tested in lithium at 1.7 Hz. Electroetched with 10 % oxalic acid.

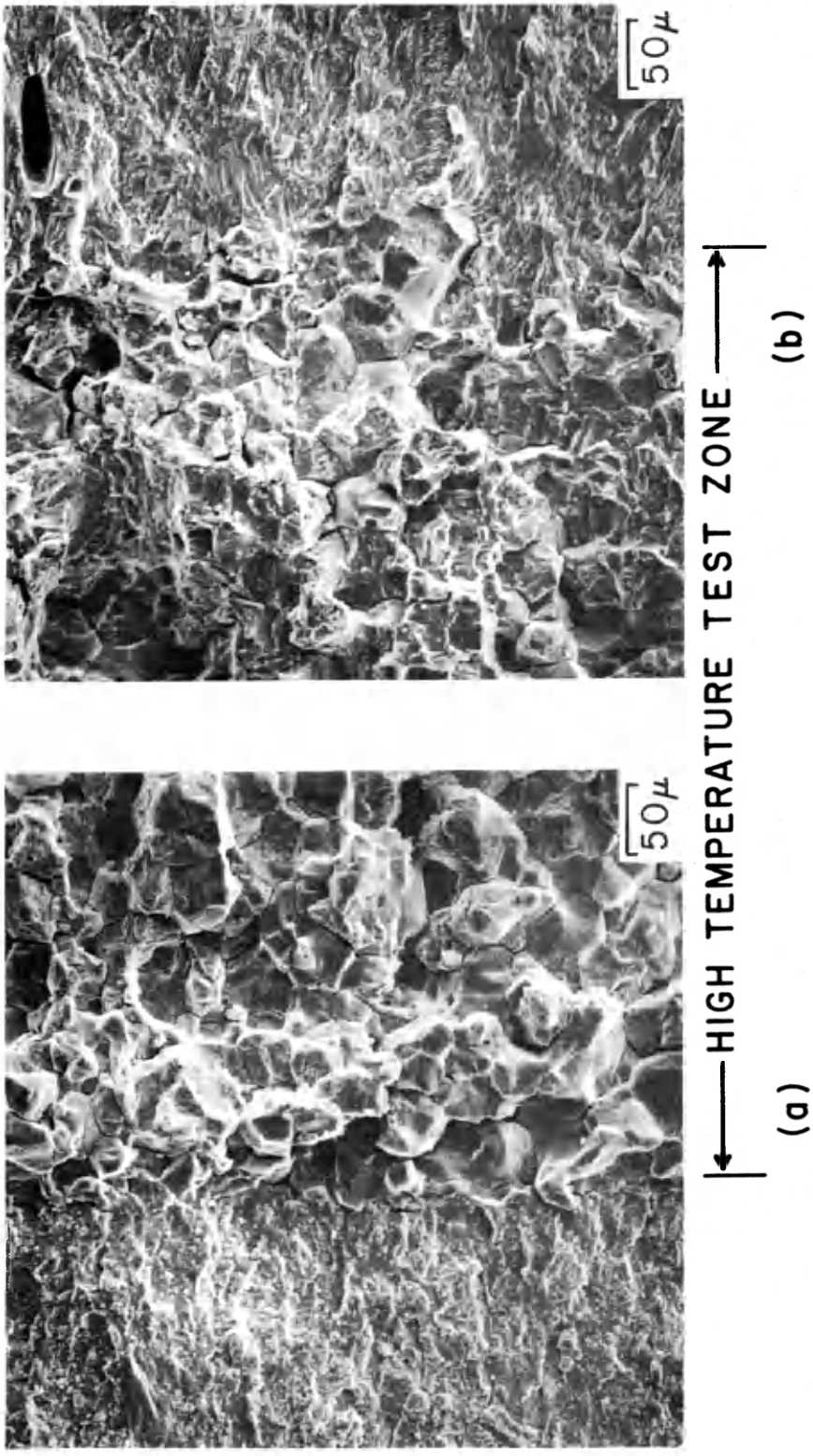

Figure 24. SEM fractographs of the area at the beginning (a) and end (b) of the high-temperature-test zone of the specimen tested in lithium at 1.7 Hz.

stainless steel can be explained in a manner analogous to that presented by Soloman and Coffin (38) in Fig. 7. The crack propagation rate increases with decreasing frequency due to an increase in the creep component of propagation which, in turn, causes intergranular crack propagation. Lithium increases the propagation rate while promoting a change from transgranular to intergranular propagation at higher frequencies. This change in propagation mode may be due to strain-enhanced grain boundary penetration similar to that reported previously for Armco iron under creep conditions (9,10).

In this analysis, it has been assumed that the argon atmosphere was an inert environment with respect to fatigue crack propagation. However, results of this investigation indicate that this was not the case for every test. The two curves presented in Fig. 20 for the growth rates in argon at 0.067 Hz are for two specimens tested under slightly different conditions. The higher growth rate occurred in a test with an upper load of 500 lb compared to 400 lb for the lower growth rate and an oxygen concentration of about 240 ppm compared to 210 ppm for the lower curve. The higher upper load caused an increase in growth rate by increasing the creep component of propagation. Although the difference in oxygen

concentration does not appear to be large, examination of the fracture surfaces suggests that this difference is significant in the 200 to 300 ppm range at 973K and that it contributed to the increase in growth rate. Figure 25 contains scanning electron micrographs of the fracture surfaces of both of the 0.067 Hz specimens tested in argon. These fractographs, both at the same magnification, show a marked difference in the nature of what is presumed to be an oxide formed at approximately 240 and 210 ppm oxygen. The high growth rate specimen in Fig. 25 (a) has a heavy oxide with well developed crystals completely obscuring the surface. Figure 25 (b), on the other hand, shows thin patches of oxide which, while almost covering the surface, do not hide the major features. The specimen tested in argon at 20 Hz showed heavy oxide formed at 280 ppm oxygen and the specimen at 1.7 Hz showed a light oxide formed at about 200 ppm oxygen. If the presence of oxygen in the argon does, in fact, increase the growth rate as proposed for 0.067 Hz (and as suggested by Fig. 7), the argon curve in Fig. 19 represents an upper bound to the crack growth rate in a truly inert environment.

In order to test for the strain-enhanced penetration proposed earlier, precracked CT specimens, identical to those used in the fatigue studies, were held at constant

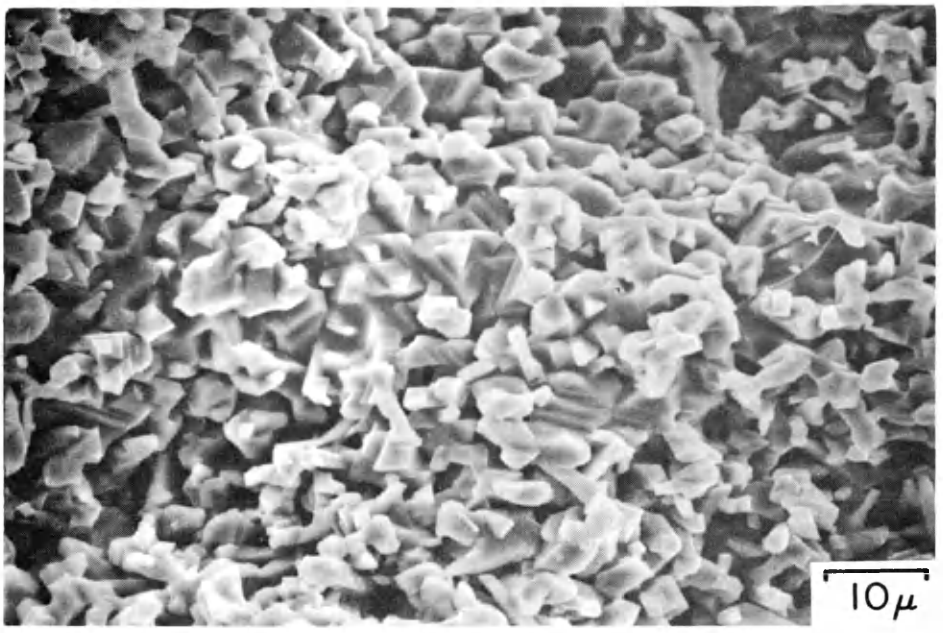

(a)

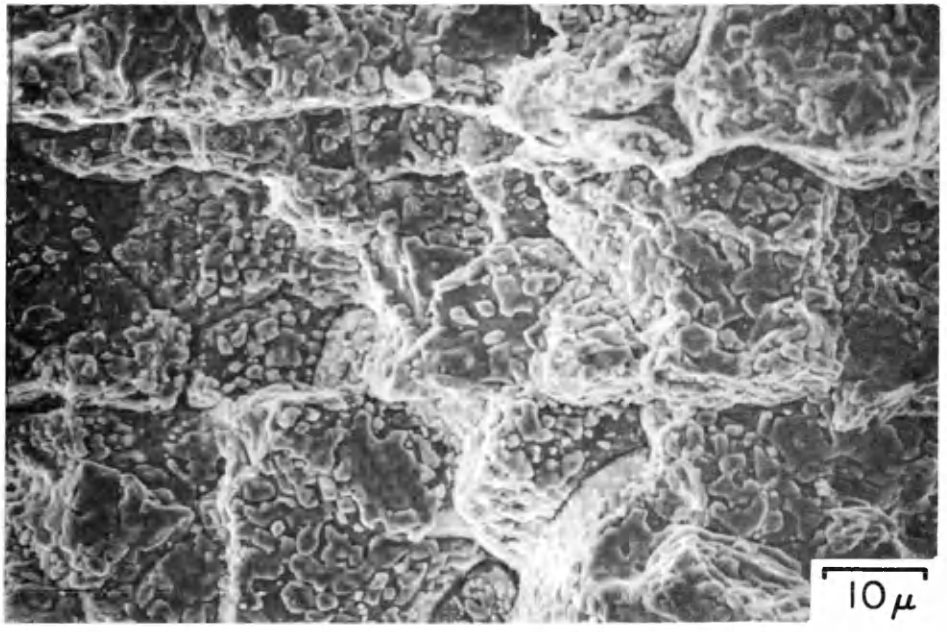

(b)

Figure 25. SEM micrographs of the oxide formed on the two specimens tested at 0.067 Hz in argon. The high growth rate specimen is shown in (a) and low growth rate in (b).

load at 973K in lithium and in argon. The load was equal to the peak load used during fatigue testing (400 lb) and the time of the test (68hr) was chosen to give measurable penetration in unstressed regions while minimizing the crack opening.

Sections of the sample tested in lithium were examined for grain boundary penetration in unstressed regions as well as at the crack tip. Figure 26 contains optical micrographs from the various points on the sample indicated in Fig. 26(d). Figure 26(a) illustrates the penetration observed on the specimen surface which was hand ground prior to testing. This penetration is comparable to that for the precrack zone through which the fatigue crack passed at room temperature prior to testing (Fig. 26(b)). The magnitude of this penetration is very close to the 78μ predicted by Equation [4] for N=0.2, T=973K, and t=68hr. A marked increase in penetration was observed for the side of the pin hole which was loaded in compression during precracking and testing as shown in Fig. 26(c). Sections from machined surfaces which were not stressed during testing showed penetrations very similar to (a) and (b). Fig. 26 (c) is qualitative evidence of strain-enhanced penetration similar to that reported for Armco iron (9,10).

Low magnification micrographs of the constant load

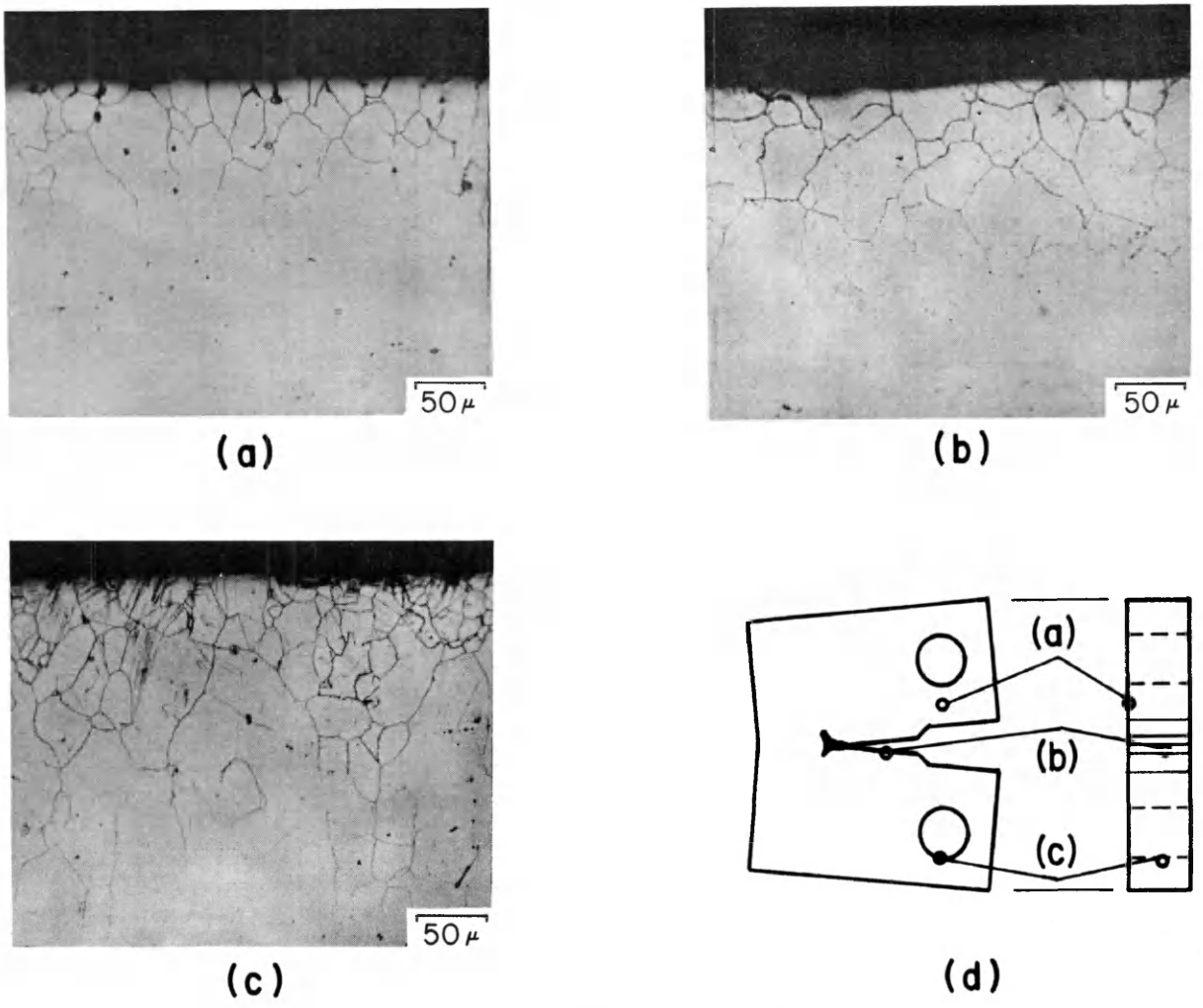

Figure 26. Optical micrographs showing the penetration observed in a specimen held in lithium for 68 hours at a constant load. As shown in (d), (a) is the hand ground surface, (b) is the fatigue precrack zone, and (c) is the side of the pin hole which was loaded during exposure. Etched with 5g $FeCl_3$, 2ml HCl, 96ml ethanol.

samples revealed the expected results as shown in the crack tip micrographs presented in Fig. 27. Dark field illumination was used to accentuate the penetration in these lightly etched samples. Figure 27 (a) shows no grain boundary attack other than a few regions where a second phase, presumably oxide, was present at the grain boundaries of the specimen tested in argon. Figure 27 (b) on the other hand, shows a uniform zone of grain boundary attack along the precrack zone with greater penetration in the region near the tip of the crack which was stressed while submerged in lithium.

Figure 27 shows that crack extensions due to normal, high-temperature creep processes at the crack tip during the constant load test in argon and in lithium were about the same. This is not indicative of the effects of the two environments, however. The initial applied K_I in the argon test was 11.4 MPa$\sqrt{m}$ and that for the lithium test was about 10.4 MPa$\sqrt{m}$. This difference in K_I, which was the result of different initial crack lengths, means that the crack tip in the argon test was under a higher stress which, in turn, caused a higher creep rate. The higher creep rate is manifested in a greater crack opening as evidenced in Fig. 27. The effect of lithium increasing crack propagation is evidenced by three observations:

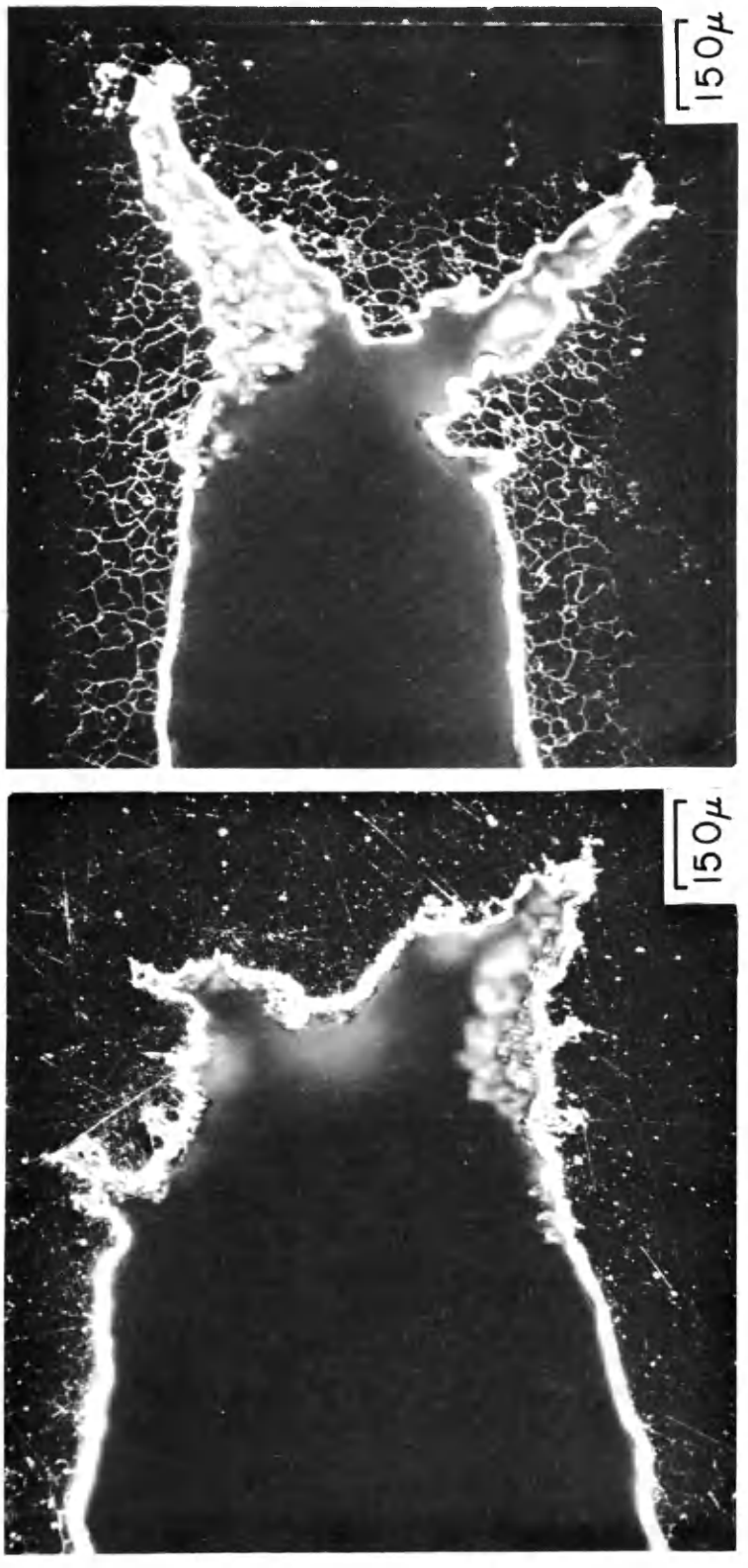

Figure 27. Dark field micrographs of the crack tips of the specimens held at a constant load of 400 lb (1980 N) in argon (a) and lithium (b). Etched with 5g FeCl , 2ml HCl, 96ml ethanol.

1) equal crack extensions with a lower applied stress in lithium,

2) equal crack extension with less deformation (crack tip opening) in lithium, and

3) two cracks propagating to approximately the same length in lithium compared to only one major crack in argon.

It is expected that the effect of propagating two cracks simultaneously is to lower the effective K_I for each crack.

Figure 27(b) and Fig. 26(c) contain evidence for strain-enhanced pentration under tensile and compressive loading. The mechanism for this phenomena is not understood but it may be the same as that for Armco iron under creep conditions. It is doubtful that a film-rupture mechanism would apply as plastic deformation in compression would tend to close grain boundaries inhibiting further penetration, especially if a corrosion product were formed. It is more likely that deformation enhances diffusion by creating excess vacancies, by producing dislocations for pipe diffusion, or by increasing grain boundary diffusivity due to grain boundary sliding.

The basis of the model for enhanced fatigue-crack propagation in the presence of liquid lithium proposed here is that grain boundary penetration, due to corrosion

processes, adds directly to the mechanical propagation which occurs in the absence of an aggressive environment. This model does not require strain enhancement of the grain boundary attack but it would contribute directly to the magnitude of the fatigue-crack acceleration observed. Due to the net tensile stress imposed during fatigue loading, fatigue cracks open during testing. This allows the bulk lithium to penetrate to very near the tip of the crack by bulk fluid flow which keeps the distance between the point of maximum penetration and the bulk lithium very small (on the order of the grain size). The distance to the point of penetration is very important as this controls the rate of penetration (dP/dt) at any given time, if a diffusion controlled model for penetration is assumed.

If it is assumed that the crack advances to the limit of penetration during each cycle, the penetration for the next cycle can apparently be calculated from Equation [4] (neglecting strain-enhanced penetration). Table II lists calculated values of penetration per cycle for each frequency tested as well as the measured crack growth rates for argon and lithium and the difference between the two growth rates. The difference in crack growth rates is about the same as the predicted penetration per cycle. For example, at 1.7 Hz the crack growth rate in lithium is

TABLE II

FREQUENCY (Hz), TIME (hr)	PENETRATION m per cycle	da/dN (m) argon	da/dN (m) lithium	Δ(da/dN) (m)
0.067, 4.15×10^{-3}	6.07×10^{-7}	2.68×10^{-7} 9.71×10^{-7}	8.21×10^{-7}	5.53×10^{-7} -1.5×10^{-7}
1.7, 1.63×10^{-4}	1.21×10^{-7}	1.27×10^{-7}	2.49×10^{-7}	1.22×10^{-7}
20, 1.39×10^{-5}	3.52×10^{-8}	6.88×10^{-8}	1.39×10^{-7}	7.02×10^{-8}

Table II. A comparison of the growth rates in argon and lithium at 14 MPa$\sqrt{m}$ with the penetration predicted from Equation [4].

1.22×10^{-7} m/cycle greater than in argon at 14MPa$\sqrt{m}$. The penetration per cycle (that for 1.63×10^{-4} hr) predicted by Equation [4] is 1.21×10^{-7} m.

These calculations suggest that the enhanced fatigue-crack-growth rate in lithium can be explained by the addition of grain boundary penetration, due to corrosion, to the growth rate in argon according to the following equation:

$$da/dN(Li) = da/dN(Argon) + da/dt \times dt/dN \qquad [9]$$

where da/dt is the penetration rate and dt/dN is the inverse of the frequency. The difference in crack growth rates, which must be equal to (da/dtxdt/dN) in this model, is a function of stress-intensity range as well as frequency as can be seen from Figures 16, 17, and 18. This is not predicted by the above equation unless da/dt is replaced by a function of ΔK. If strain-enhanced penetration is considered, the penetration rate would become a function of ΔK. The assumption that the crack opens to the limit of penetration, and that Equation [4] can be applied to very short times, will now be discussed .

If the penetrated grain boundary maintained some integrity as reported by Popovich et al (15) for Armco iron, the crack may not open to the limit of penetration. This would decrease the penetration rate by increasing the

distance from the bulk lithium to the penetration point. The length of penetrated boundary not opened may be a function of frequency.

The application of Equation [4] for short times, as in Table II, may not be correct as a delay time is observed in the grain boundary attack of 304L stainless steel (5). This delay time, which was not incorporated into Equations [2] and [4], was interpreted as the time for formation of a corrosion product or a precipitate. It may, however, indicate that extrapolation of the measured penetration data to zero penetration on a parabolic time plot is not valid. A change in kinetics from linear time to parabolic time dependence as penetration approaches a critical distance would allow penetration to begin at zero time. This is shown schematically in Fig. 28 which is a plot of penetration rate as a function of time for penetration proportional to t and $t^{1/2}$ and of penetration versus $t^{1/2}$. If the two processes represented in Fig. 28 are dependent the slowest one in Fig. 28(a) would be rate controlling and the kinetics would change as indicated. This change in kinetics would result in an apparent delay time as shown in Fig. 28(b).

Two additional explanations for the apparent delay time are offered. The delay time may be due to the

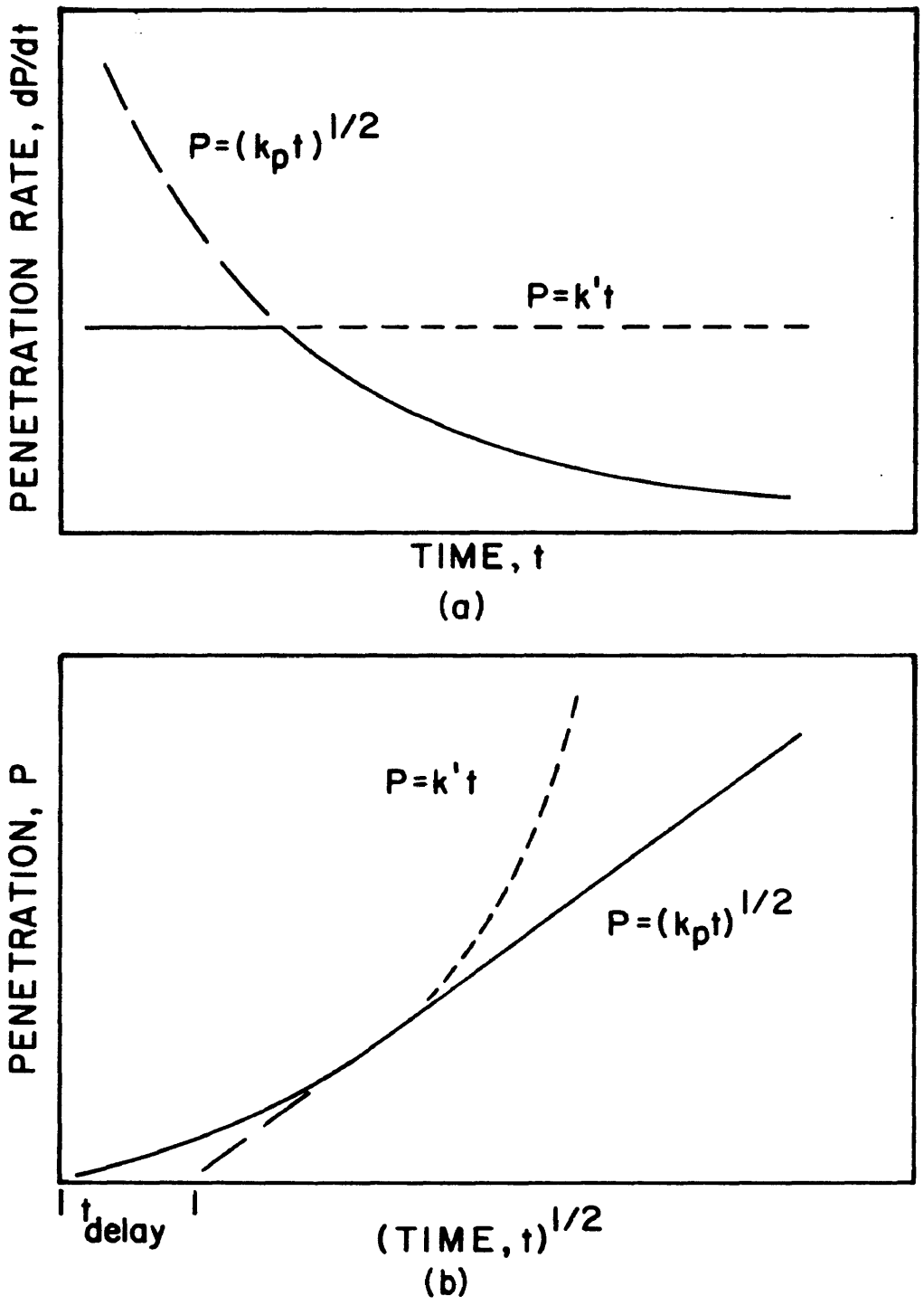

Figure 28. Schematic plots of penetration rate as a function of time (a) and penetration as a function of t (b) showing an apparent delay time when the kinetics change from linear to parabolic (the solid line in both figures).

dissolution of a surface film such as the passive oxide layer on stainless steel. Optical metallography would not be able to detect this process and an apparent delay time would result. During fatigue crack propagation, a surface film would not form and the dissolution process would not need to occur. The second explanation involves uniform surface attack. If this surface attack was initially as rapid as the grain boundary attack, no penetration would be measured. Surface attack would not lead to intergranular crack propagation and, therefore, does not apply here.

The preceding paragraphs show that the application of Equation [4] under the conditions at the tip of a propagating fatigue crack is not justified. However, the data presented in Table II suggest that modification of this equation, to correct for the effects of strain and short times, should not alter the results drastically. Unfortunately, no techniques have been developed which can accurately resolve grain boundary penetration in the short duration of a fatigue cycle (1 to 0.05 sec). This prevents a critical analysis of the proposed mechanism of penetration preceding crack propagation which adds directly to the mechanical growth.

The question of which material property (corrosion or fatigue resistance) controls the rate of fatigue crack

propagation in a lithium environment is significant. If the rate of propagation is controlled by the amount of penetration at the crack tip, the corrosion resistance of the material will be important as will parameters which influence the corrosion process (eg. nitrogen in the lithium). If the rate of propagation is controlled primarily by the fatigue resistance of the material, the corrosion resistance and nature of the lithium environment will be of secondary importance. This is a major consideration in that it may ultimately decide the selection criteria (corrosion or fatigue resistance) for lithium container materials. An investigation of the influence of temperature and nitrogen in the lithium on da/dtxdt/dN would be useful in further analysis.

CONCLUSIONS

(1) The fatigue-crack-propagation rate of 304L stainless steel in lithium was found to be greater, by a factor of approximately 2, than the rate in an argon atmosphere at 973K and at frequencies of 20, 1.7, and 0.067 Hz.

(2) The increase in fatigue-crack-propagation rate was accompanied by a change in propagation mode from transgranular in argon, to intergranular in lithium at 20 and 1.7 Hz as shown by scanning electron microscopy and optical metallography. The propagation mode was intergranular in both environments at 0.067 Hz. No change in propagation mode during any single test was observed.

(3) The effect of frequency was as expected with propagation rate increasing with a decrease in frequency

and propagation mode changing from transgranular to intergranular for specimens tested in argon.

(4) The slopes of the da/dN vs. ΔK curves for specimens tested in lithium were greater than for the corresponding specimens tested in argon at all frequencies. This suggests that the effects of lithium are greater at higher values of stress-intensity-factor range.

(5) Qualitative evidence for strain-enhanced penetration by liquid lithium in 304L stainless steel was obtained from constant load tests.

(6) Evidence for increasing propagation rates with increasing oxygen concentration (for the argon environment tests) indicates that the argon data for this investigation represents an upper bound for propagation in a truly inert environment.

(7) On the basis of the experimental observations of this investigation, a model for lithium-enhanced, fatigue crack propagation is proposed. Grain boundary penetration by liquid lithium at the tip of a propagating fatigue crack adds directly to the mechanical propagation. Strain-

enhanced penetration is necessary to explain greater enhancement at higher ΔK values. No data on grain-boundary-penetration rates for very short times (ie. 0.05 sec), with or without an applied stress, is available to critically evaluate this model.

(8) Additional studies are needed to determine the influence of impurities (ie. nitrogen in the lithium) and temperature on the effects of lithium and frequency on the fatigue- crack-propagation characteristics of 304L stainless steel.

REFERENCES

1. D. L. Olson and D. K. Matlock; Energy, Vol. 3, 1978, p. 315-323.

2. P. A. Steinmeyer, D. L. Olson, G. R. Edwards, and D. K. Matlock; Review on Coatings and Corrosion, in press, 1980.

3. E. E. Hoffman; ORNL-22674. 1959.

4. D. L. Olson, G. N. Reser, and D. K. Matlock; Corrosion, in press, 1980.

5. R. A. Patterson and D. L. Olson; Nucl. Mat. Vol. 57, 1975, p. 312.

6. R. J. Schlager; Nucl. Tech., Vol. 29, 1976, p. 94.

7. J. A. Reeves, D. L. Olson, and W. L. Bradley; Nucl. Tech., Vol. 30, 1976, p.385.

8. J. E. Selle; Proc. of Int. Conf. on Liquid Metal Technology in Energy Production, ANS-AIME Conf. Proc. No. CONF-760503-P2, Champion, Pa., 1976, p. 453.

9. W. Jordan, W. L. Bradley, and D. L. Olson; Nucl. Tech., Vol. 29, 1976, p. 209-214.

10. T. A. Whipple, D. L. Olson, W. L. Bradley, and D. K. Matlock; Nucl. Tech., Vol. 39, 1978, p. 75-83.

11. F. M. Kustas; Master of Science Thesis, No. T2097, Colorado School of Mines, Golden, Colo., 1978.

12. D. Bates, G. R. Edwards, and D. L. Olson; NACE 79,

paper 118, Atlanta, Ga., 1979.

13. P. Steinmeyer; unpublished research, Colorado School of Mines, Golden, Colo., 1980.

14. J. A. Reeves,Jr., D. L. Olson, and W. L. Bradley; Nucl. Tech, Vol. 30, 1976, p. 385-389.

15. V. V. Popovich, I. G. Shtydalo, and M. I. Chaevskii; Sov. Mat. Science, Vol. 3, No. 2, 1967, p. 127-133.

16. M. I. Chaevskii and V. V. Popovich; Sov. Mat. Science, Vol. 3, No. 2, 1967, p. 251-256.

17. V. V. Popovich, M. S. Goikman, E. I. Polyakov, and M. I. Chaevskii; Sov. Mat. Science, Vol. 5, No. 4, 1969, p. 345-351.

18. H. Tas, F. Casteels, and M. Schirra; Proceedings of International Conference on Liquid Metal Technology in Energy Production, ANS-AIME Conf. Proc. No. CONF-76053-P1, Champion, Pa., 1976, p. 346-352.

19. H. V. Borgstedt and G. Frees; Proceedings of International Conference on Liquid Metal Technology in Energy Production, ANS-AIME Conf. Proc. No. CONF-76053-P1, Champion, Pa., 1976, p. 331-337.

20. K. Natesan, O. K. Chopra, and T. F. Kassmer; Proceedings of International Conference on Liquid Metal Technology in Energy Production, ANS-AIME Conf. Proc. No. CONF-76053-P1, Champion, Pa., 1976, p. 338-345.

21. P. N. Flagella and J. R. Kahrs; Proceedings of International Conference on Liquid Metal Technology in Energy Production, ANS-AIME Conf. Proc. No. CONF-76053-P1, Champion, Pa., 1976, p. 353.

22. D. L. Smith, G. J. Zeman, K. Natesan, and T. F. Kassner; Proceedings of International Conference on Liquid Metal Technology in Energy Production, ANS-AIME Conf. Proc. No. CONF-76053-P1, Champion, Pa., 1976, p. 359-367.

23. L. A. James and R. L. Knecht; Met. Trans., Vol. 6A, 1975, p. 109-116.

24. Stanley T. Rolfe and John M. Barsom; "Fracture and

Fatigue Control in Structures; Applications of Fracture Mechanics", Prentice-Hall Inc., Englewood Cliffs, New Jersey, 1977, p. 292-316.

25. Mars G. Fontana and Norbert D. Greene; "Corrosion Engineering", 2nd ed., McGraw Hill, 1978, p. 91-107.

26. A. J. Bursle and E. N. Pugh; from "Environment-Sensitive Fracture of Engineering Materials", Z. A. Foroulis, ed., Conference Proceedings, Chicago, Ill., Oct. 24-26, 1977, AIME, Warrendale, Pa., 1979, p. 18-47.

27. D. J. Duquette; from "Environment-Sensitive Fracture of Engineering Materials", Z. A. Foroulis, ed., Conference Proceedings, Chicago, Ill., Oct. 24-26, 1977, AIME, Warrendale, Pa., 1979, p. 521-537.

28. S. Floreen and R. J. Kane; Met. Trans, Vol 10A, 1979, p. 1745-1751.

29. P. S. Pao, W. Wei, and R. P. Wei; from "Environment-Sensitive Fracture of Engineering Materials", Z. A. Foroulis, ed., Conference Proceedings, Chicago, Ill., Oct. 24-26, 1977, AIME, Warrendale, Pa., 1979, p. 565-580.

30. S. P. Lynch; from "Fatigue Mechanisms", J. T. Fong, ed., ASTM STP 675,1979, p. 174-203.

31. N. S. Stoloff; from "Environment-Sensitive Fracture of Engineering Materials", Z. A. Foroulis, ed., Conference Proceedings, Chicago, Ill., Oct. 24-26, 1977, AIME, Warrendale, Pa., 1979, p. 486-518.

32. M. H. Kamdar; Progress in Mat. Science, Vol. 15, Pt 4, p. 289-374.

33. A. Kelly; Phil. Mag., Vol. 15, 1967, p. 567-586.

34. H. K. Birnbaum; from "Environment-Sensitive Fracture of Engineering Materials", Z. A. Foroulis, ed., Conference Proceedings, Chicago, Ill., Oct. 24-26, 1977, AIME, Warrendale, Pa., 1979, p. 326-360.

35. P. G. Shewmon; Met. Trans., Vol. 7A, 1976, p. 279.

36. R. H. Cook and A. P. Skelton; Int. Met. Reviews, Review 187, Vol. 19, 1974, p. 199-222.

37. C. Laird; from "Fatigue Crack Propagation", ASTM STP 415, 1967, p. 131-168.

38. H. D. Soloman and L. F. Coffin, Jr.; from "Fatigue at Elevated Temperatures", ASTM STP 520, 1973, p. 112-122.

39. P. Paris and F. Erdogan; Trans. Amer. Soc. Mech. Eng., Vol. 85, 1963, p. 528.

40. William F. Brown, Jr. and John E. Srawley; from "Plane Strain Crack Toughness Testing of High Strength Metallic Materials", ASTM STP 410, 1966, p. 8-16.

41. same as ref. 24, p. 208-245.

42. D. Walton and E. G. Ellison; Int. Met. Reviews, Review 163, Vol. 17, 1972, p. 100-116.

43. P. E. Irving and L. N. McCartney; Metal Science, Aug/Sept, 1977, p. 351-361.

44. H. I. McHenry, Jour. of Mat., JMSLA, Vol. 6, No. 4, 1971, p. 862-873.

45. George E. Dieter; "Mechanical Metallurgy", 2nd ed., McGraw-Hill, New York, 1976, p. 335.

46. R. J. Schlager, D. L. Olson, and W. L. Bradley; Nucl. Tech., Vol. 27, 1975, p. 439-441.

APPENDIX

This Appendix contains the data from this investigation. The measured compliances, temperature-corrected compliances, and calculated crack lengths are listed as functions of the number of cycles. Testing parameters are given for each set of data.

Table A-1:
Environment= argon; Frequency= 20 Hz;
Temperature= 973 K; Load Range= 50 to 400 lb;
Initial Crack Length= 0.583; Final Crack Length= 0.733.

Cycles (number)	Compliance (10^{-6} in/lb)	Comp x 0.68 (10^{-6} in/lb)	Crack Length (inches)
0	13.53	9.20	0.590
1000	13.07	8.89	0.571
2000	13.33	9.06	0.581
10000	13.37	9.09	0.583
20000	13.50	9.18	0.588
30000	13.77	9.36	0.599
35000	13.86	9.42	0.603
55000	15.17	10.32	0.641
56000	14.88	10.12	0.634
57000	15.20	10.34	0.642
60000	15.80	10.74	0.655
61000	15.47	10.52	0.648
63000	15.83	10.76	0.655
67000	16.60	11.29	0.669
70000	17.00	11.56	0.675
72000	17.50	11.90	0.683
73000	17.53	11.92	0.683
75000	17.97	12.22	0.689
77000	18.67	12.70	0.699
78000	19.10	12.99	0.704
79000	18.80	12.78	0.700
81000	19.60	13.33	0.710
83000	20.00	13.60	0.714
85000	21.10	14.35	0.725
87000	22.67	15.42	0.736

Table A-2:
Environment= argon; Frequency= 1.7 Hz;
Temperature= 973K; Load Range= 50 to 450 lb;
initial Crack Length= 0.603; Final Crack Length= 0.721.
Note: The load range was changed at 16000 cycles so the earlier data has been omitted.

Cycles (number)	Compliance (10^{-6} in/lb)	Comp x 0.77 (10^{-6} in/lb)	Crack Length (inches)
16000	11.73	9.03	0.579
18000	11.96	9.21	0.590
21000	11.94	9.19	0.589
24000	11.98	9.22	0.591
26000	12.43	9.57	0.610
29000	12.49	9.62	0.613
31000	12.70	9.78	0.620
33000	13.14	10.12	0.634
35000	13.35	10.28	0.639
37000	13.56	10.44	0.645
39000	14.45	11.13	0.665
40500	14.72	11.33	0.670
41500	15.04	11.58	0.676
43000	15.69	12.08	0.686
44000	15.86	12.21	0.689
45000	16.43	12.65	0.698
46000	17.11	13.17	0.707
47000	17.44	13.43	0.711
48000	17.79	13.70	0.716
49000	18.62	14.34	0.725

Table A-3:
Environment= argon; Frequency= 0.067 Hz;
Temperature= 973 K; Load Range= 50 to 500 lb;
Initial Crack Length= 0.574; Final Crack Length= 0.713.

Cycles (number)	Compliance (10^{-6} in/lb)	Comp x 0.77 (10^{-6} in/lb)	Crack Length (inches)
0	11.86	9.13	0.586
100	11.61	8.94	0.573
200	11.73	9.03	0.579
500	11.70	9.01	0.577
1000	12.19	9.39	0.600
1625	13.50	10.40	0.644
1800	13.51	10.40	0.644
2000	14.19	10.93	0.660
2500	14.82	11.41	0.672
2750	15.39	11.85	0.682
2900	16.36	12.60	0.697
3000	16.47	12.68	0.698

Table A-4:
Environment= argon; Frequency= 0.067 Hz;
Temperature= 973 K; Load Range= 50 to 400 lb;
Initial Crack Length= 0.570; Final Crack Length= 0.687.

Cycles (number)	Compliance (10^{-6} in/lb)	Comp x 0.78 (10^{-6} in/lb)	Crack Length (inches)
0	11.97	9.4	0.602
100	11.89	9.3	0.596
200	11.49	9.0	0.576
500	11.05	8.6	<0.550
1000	11.18	8.7	0.550
1500	11.06	8.6	<0.550
2500	11.23	8.8	0.562
3000	11.36	8.9	0.570
3500	11.36	8.9	0.570
4700	11.49	9.0	0.576
5000	11.61	9.1	0.583
5750	11.60	9.0	0.576
6500	11.78	9.2	0.590
7000	12.13	9.5	0.606
7750	12.19	9.5	0.606
9000	12.41	9.7	0.616
10500	13.06	10.2	0.636
10750	13.04	10.2	0.636
11250	13.12	10.2	0.636
12000	13.64	10.6	0.650
12500	13.53	10.6	0.650
13000	13.75	10.7	0.653
14000	14.40	11.2	0.666
14500	14.48	11.3	0.669
15000	14.57	11.4	0.672
16050	15.40	12.0	0.685

Table A-5:
Environment= lithium; Frequency= 20 Hz;
Temperature= 973 K; Load Range= 50 to 380 lb;
Initial Crack Length= 0.570; Final Crack Length= 0.683.

Cycles (number)	Compliance (10^{-6} in/lb)	Comp x 0.71 (10^{-6} in/lb)	Crack Length (inches)
0	12.71	9.02	0.578
1000	12.44	8.83	0.565
5000	12.18	8.65	0.550
20000	12.28	8.72	0.556
30000	12.96	9.20	0.590
40000	14.09	10.00	0.629
42000	14.30	10.15	0.635
45000	14.72	10.45	0.645
48000	15.35	10.90	0.659
51000	16.14	11.46	0.673
53000	17.30	12.28	0.690

Table A-6:
Environment= lithium; Frequency= 1.7 Hz;
Temperature= 973 K; Load Tange= 50 to 400 lb;
Initial Crack Length= 0.563; Final Crack Length= 0.675.

Cycles (number)	Compliance (10^{-6} in/lb)	Comp x 0.74 (10^{-6} in/lb)	Crack Length (inches)
0	11.93	8.79	0.561
500	11.96	8.81	0.564
1000	11.76	8.67	0.551
3000	11.24	8.28	<0.550
8000	11.32	8.34	<0.550
12000	11.52	8.49	<0.550
16000	11.82	8.71	0.556
19000	12.36	9.11	0.584
21000	12.45	9.18	0.589
23000	12.83	9.46	0.604
25000	13.47	9.93	0.627
26500	13.74	10.13	0.634
28000	14.13	10.41	0.644
29000	14.90	10.98	0.661
30000	15.10	11.13	0.665
30500	15.28	11.26	0.668
31000	15.67	11.55	0.675
31500	15.78	11.63	0.677

Table A-7:
Environment= lithium; Frequency= 0.067 Hz;
Temperature= 973 K; Load Range= 50 to 450 lb;
Initial Crack Length= 0.562; Final Crack Length= 0.687.
Note: The load range was changed at 5000 cycles so the earlier data has been omitted.

Cycles (number)	Compliance (10^{-6} in/lb)	Comp x 0.86 (10^{-6} in/lb)	Crack Length (inches)
5000	9.08	7.81	<0.550
5200	9.22	7.93	<0.550
5500	9.10	7.83	<0.550
6000	9.24	7.95	<0.550
7000	9.30	8.00	<0.550
7500	9.30	8.00	<0.550
8500	9.41	8.09	<0.550
11500	9.78	8.41	<0.550
13000	9.74	8.38	<0.550
15000	10.18	8.75	0.559
17000	11.55	9.93	0.627
18000	11.98	10.30	0.640
18500	12.66	10.89	0.659
18900	12.67	10.90	0.659
19000	12.79	11.00	0.662
19408	14.29	12.29	0.691
19425	14.05	12.08	0.686